

Combined constraints on dark photons from high-energy collisions, cosmology, and astrophysics

A. W. Romero Jorge,^{1, 2, 3, *} L. Sagunski,² Guan-Wen Yuan,^{4, 5} T. Song,⁶ and E. Bratkovskaya^{6, 2, 3}

¹*Frankfurt Institute for Advanced Studies (FIAS),
Ruth Moufang Str. 1, 60438 Frankfurt, Germany*

²*Institut für Theoretische Physik, Johann Wolfgang Goethe University,
Max-von-Laue-Str. 1, 60438 Frankfurt, Germany*

³*Helmholtz Research Academy Hessen for FAIR (HFHF),
GSI Helmholtz Center for Heavy Ion Physics, Campus Frankfurt, 60438 Frankfurt, Germany.*

⁴*Department of Physics, University of Trento, Via Sommarive 14, 38123 Povo (TN), Italy*

⁵*Trento Institute for Fundamental Physics and Applications (TIFPA)-INFN, Via Sommarive 14, 38123 Povo (TN), Italy*

⁶*GSI Helmholtzzentrum für Schwerionenforschung GmbH, Planckstraße 1, 64291 Darmstadt, Germany*

(Dated: January 22, 2026)

We investigate a dark sector coupled to the Standard Model (SM) through a kinetically mixed dark photon U associated with a new $U(1)'$ gauge symmetry. Kinetic mixing, parametrized by ε , induces an effective coupling to the electromagnetic current, while the dark photon interacts with a stable dark matter (DM) particle χ through a dark gauge coupling g_χ , defining a four-dimensional parameter space $(m_U, \varepsilon, m_\chi, g_\chi)$. Our analysis is based on the parton–hadron–string dynamics (PHSD) transport approach, extended to include dark photon production and decay into dileptons ($U \rightarrow e^+ e^-$). In PHSD, dark photons are produced in high-energy collisions through Dalitz decays of light mesons ($\pi^0, \eta, \eta', \omega$), Delta-resonances ($\Delta \rightarrow NU$), direct vector meson decays ($\rho, \omega, \phi \rightarrow U$), kaon decays ($K^+ \rightarrow \pi^+ U$), and $q\bar{q} \rightarrow U$ annihilation. Building on previous PHSD benchmarks against dilepton data, we extract upper limits on $\varepsilon^2(m_U, m_\chi, \alpha_\chi)$ in both the visible regime ($m_U < 2m_\chi$), where $U \rightarrow e^+ e^-$ dominates, and the invisible regime ($m_U > 2m_\chi$), where $U \rightarrow \chi\bar{\chi}$ is kinematically open and suppresses the dilepton branching fraction. Cosmological and astrophysical constraints are incorporated in two complementary ways. First, we compute the velocity-dependent self-interaction cross section σ/m_χ for Yukawa-mediated SIDM and confront it with bounds from dwarf galaxies, galaxy groups, and clusters. Second, we determine thermal relic target curves by computing the relic abundance and requiring $\Omega_{\text{DM}} h^2 \simeq 0.12$, consistent with *Planck* measurements of the cosmic microwave background. Combining PHSD limits on ε^2 with relic density and self-interaction requirements, we exclude regions of the (m_χ, m_U) plane for each DM realization (Dirac fermion, Majorana fermion, or complex scalar) and identify benchmark scenarios in which heavy-ion, cosmological, and astrophysical constraints are simultaneously satisfied.

I. INTRODUCTION

Dark matter (DM) is an essential ingredient of the standard cosmological model: fits to the cosmic microwave background (CMB), large-scale structure, and other cosmological probes imply that roughly one quarter of the total energy density of the Universe resides in a non-luminous, non-baryonic component that interacts predominantly via gravity [1]. Its presence is required across a wide range of length scales. On galactic scales, stellar kinematics and neutral-hydrogen rotation curves show that the circular velocity of spiral galaxies remains approximately flat far beyond the visible stellar disc, pointing to extended DM halos [2, 3]. In galaxy clusters, strong and weak gravitational lensing in merging systems such as the Bullet Cluster and Abell 520 reveals that most of the mass is collisionless and spatially separated from the X-ray emitting intracluster gas [4, 5]. Taken together, these observations robustly motivate new degrees of freedom beyond the Standard Model (SM).

At the same time, high-resolution N -body simulations of cold, collisionless DM exhibit tensions with observations on sub-galactic scales. Cuspy inner density profiles and an overabundance of massive subhalos predicted in Λ CDM do not always match the cored density profiles and satellite populations of dwarf and low-surface-brightness galaxies [6]. Self-interacting dark matter (SIDM), in which DM particles undergo elastic scattering with cross section per unit mass $\sigma/m_\chi \sim 0.1\text{--}10 \text{ cm}^2 \text{ g}^{-1}$, provides a simple and well-motivated extension of Λ CDM that can alleviate the core–cusp and too-big-to-fail problems without spoiling its large-scale successes [7, 8]. In realistic models, this often arises from a light mediator generating a Yukawa potential, which naturally leads to a velocity-dependent cross section: large at the low velocities of dwarf galaxies, and suppressed in the high-velocity regime characteristic of galaxy groups and clusters.

Cosmology provides a complementary and independent handle on DM properties. The CMB temperature and polarization anisotropies measured by *Planck* tightly constrain the present-day DM relic density to $\Omega_{\text{DM}} h^2 \simeq 0.12$ [1, 9]. In thermal scenarios, this value is reproduced if the total (co)annihilation rate of DM in the early Universe is of order $\langle \sigma v \rangle \sim 10^{-26} \text{ cm}^3 \text{ s}^{-1}$

* jorge@itp.uni-frankfurt.de

[10], thereby linking cosmological observations to the microscopic couplings of the dark sector. Any viable model must therefore accommodate both the relic density requirement and the astrophysical constraints on self-interactions.

Despite intense efforts, direct and indirect searches have not yet yielded a conclusive detection of DM. Underground detectors probing nuclear and electronic recoils, γ -ray and cosmic-ray observations of the Galactic halo, and collider searches at the LHC have excluded large regions of parameter space, but still leave ample room for light mediators and non-minimal dark sectors. This motivates exploring frameworks in which the same mediator controls early-Universe annihilation, potential self-interactions, and laboratory signatures.

A minimal and well-motivated way to couple a dark sector to the Standard Model (SM) is via renormalizable *portals* [11–14]. These are dimension-four operators that connect SM fields to new gauge-singlet degrees of freedom. In this work we focus on the vector portal, in which a new Abelian $U(1)'$ gauge boson kinetically mixes with hypercharge. The interaction $\mathcal{L} \supset \frac{\varepsilon}{2} B_{\mu\nu} F'^{\mu\nu}$ first proposed by Holdom [15] induces a coupling of the associated gauge boson, often referred to as a dark photon, hidden photon, or U boson to the electromagnetic current with strength εe . The dark photon can acquire a mass m_U through a Stueckelberg term or a dark Higgs mechanism, and its coupling to charged SM particles is then set by ε^2 , which controls its partial widths into e^+e^- , $\mu^+\mu^-$, and hadronic states [16–21]. For ε in the range 10^{-7} – 10^{-2} such states can be long-lived yet remain compatible with precision electroweak data, while still being accessible to dedicated searches.

An important phenomenological advantage of the vector portal is that a dark photon can be radiated from any electromagnetic current. In the low-mass region, this implies a rich set of hadronic production channels: Dalitz decays of light pseudoscalars (π^0, η, η'), radiative decays of baryon resonances such as $\Delta \rightarrow N\gamma^*$, and direct conversions of vector mesons ρ, ω , and ϕ . Searches typically look for a narrow resonance in the dilepton invariant-mass spectrum above the smooth SM background [22–24]. A broad experimental programme ranging from fixed-target and beam-dump experiments to flavor factories and LHC detectors has excluded $\varepsilon^2 \gtrsim 10^{-6}$ for dark photon masses between a few tens of MeV and several GeV [25–37]. Nevertheless, important gaps remain, in particular near the ρ, ω , and ϕ resonances and in regions where laboratory, beam-dump, and astrophysical constraints lose sensitivity.

Heavy-ion collisions offer a complementary window on the vector portal. They create hot and dense strongly interacting matter, produce a large number of light mesons and baryon resonances, and, at collider energies, form a thermalized quark-gluon plasma (QGP). Both the hadronic and partonic stages emit virtual photons and, in the presence of kinetic mixing, dark photons, which subsequently decay into dileptons. In our previous stud-

ies, we implemented this mechanism within the parton-hadron-string dynamics (PHSD) transport framework to derive upper limits on $\varepsilon^2(m_U)$ in the *visible* regime, where the decay $U \rightarrow e^+e^-$ dominates and the dark channel is kinematically inaccessible. Those works focused on dark photons produced through hadronic and partonic sources, demonstrating that high-precision dilepton spectra from $p + p$, $p + A$, and $A + A$ collisions provide a competitive probe of dark photons across the MeV-GeV range [38–41].

In the present work, we embed this dark photon phenomenology into a more general dark sector framework and substantially extend the scope of the analysis. We consider a dark photon coupled to a stable DM particle χ with dark gauge coupling g_χ , exploring both fermionic (Dirac and Majorana) and complex scalar realizations. The resulting parameter space $(m_U, \varepsilon, m_\chi, g_\chi)$ links heavy-ion observables to cosmology and astrophysics through thermal freeze-out and self-interacting DM dynamics. Our main advances compared to our previous PHSD study [42] are:

- (i) **Visible and invisible regimes:** we extend the PHSD-based extraction of $\varepsilon^2(m_U)$ to the invisible regime where $U \rightarrow \chi\bar{\chi}$ is open, deriving upper limits on the kinetic mixing.
- (ii) **Astrophysical self-interaction constraints:** we compute the velocity-dependent self-interaction cross section σ/m_χ using CLASSICS and confront it with SIDM bounds from dwarf galaxies, galaxy groups, and clusters, thereby excluding portions of the (m_χ, m_U) plane where self-interactions are either too weak to alleviate small-scale tensions or too strong to be compatible with high-velocity systems.
- (iii) **Thermal relic targets and invisible limits:** employing RED-DELIVER, we determine thermal relic target curves in $(m_\chi, m_U, \varepsilon, g_\chi)$ space for Dirac, Majorana, and complex scalar DM, and combine them with our PHSD limits on the invisible kinetic mixing to rule out parts of the parameter space where a standard thermal history would require a mixing already excluded by heavy-ion dilepton data.
- (iv) **Benchmark scenarios:** we identify three representative benchmark points in the (m_χ, m_U) plane that simultaneously satisfies heavy-ion, cosmological, and astrophysical constraints, and are thus particularly promising targets for future experimental searches.

The paper is structured as follows. In Sec. II, we introduce the dark photon framework with a generic dark sector, specifying the kinetic mixing Lagrangian, the dark currents, and mass terms for Dirac, Majorana, and complex scalar dark matter, and the resulting visible and invisible partial widths and branching ratios. In Sec. III,

we summarize the PHSD transport approach and its implementation of standard model dilepton sources, and we describe how dark photons are produced in hadronic and partonic channels, and how visible and invisible limits on $\varepsilon^2(m_U)$ are extracted from dilepton spectra. Section IV is devoted to self-interacting dark matter: we compute Yukawa-mediated self-interaction cross sections with CLASSICS, construct the effective cross section $\sigma_{\text{eff}}/m_\chi$, and compare to astrophysical constraints from dwarfs, galaxies, groups, and clusters. In Secs. V and VA we discuss the thermal relic abundance, use RED-DELiVER to obtain thermal relic target curves for the different DM spins, and derive their scaling in the non-relativistic limit. In Sec. VI we combine heavy-ion, cosmological, and astrophysical constraints in the (m_χ, m_U) plane, identify regions where thermal targets are excluded by invisible PHSD limits, and define three representative benchmark scenarios. Finally, Sec. VII summarizes our main results and outlines prospects for future experimental tests. We work in natural units $\hbar = c = k_B = 1$ unless stated otherwise. Masses are quoted in MeV/GeV, velocities in km s^{-1} , and self-interaction cross sections per unit mass in $\text{cm}^2 \text{g}^{-1}$.

II. MODELING OF DARK PHOTON PRODUCTION WITH A GENERIC DARK SECTOR

A minimal and well-motivated way to couple a hidden sector to the Standard Model (SM) is through renormalizable *portals*, i.e. dimension-four operators linking SM fields to new gauge-singlet degrees of freedom. Prominent examples include the Higgs portal (spin-0 scalar mediator), the neutrino portal (spin-1/2 singlet fermion), the axion/pseudoscalar portal (spin-0 pseudoscalar), and the *vector portal*, in which a new Abelian spin-1 gauge boson kinetically mixes with hypercharge [11, 15, 20, 43]. In this work we focus on the vector portal. At energies well below the Z mass, kinetic mixing induces an effective coupling of the dark photon U to the electromagnetic current with strength εe .

To allow for invisible decays of the mediator, we consider a generic dark sector containing a particle charged under a dark $U(1)'$ gauge symmetry. We assume an elastic setup with a single stable dark sector state χ (or φ for a complex scalar field), so that invisible decays proceed dominantly via $U \rightarrow \chi\bar{\chi}$ (or $U \rightarrow \varphi\varphi^\dagger$) when kinematically allowed. The interaction strength is parametrized by g_χ (or equivalently $\alpha_\chi \equiv g_\chi^2/4\pi$), and the minimal renormalizable Lagrangian is

$$\mathcal{L} = \mathcal{L}_{\text{SM}} - \frac{1}{4} F'_{\mu\nu} F'^{\mu\nu} + \frac{\varepsilon}{2} B_{\mu\nu} F'^{\mu\nu} + \frac{1}{2} m_U^2 A'_\mu A'^\mu - g_\chi A'_\mu J_\chi^\mu + \mathcal{L}_{\text{mass}}^X, \quad (1)$$

where $B_{\mu\nu}$ and $F'_{\mu\nu}$ denote the hypercharge and dark field strength tensors, respectively. The dark photon field is A'_μ and its mass is m_U . Throughout, we parametrize the

dark sector interaction strength by $\alpha_\chi \equiv g_\chi^2/(4\pi)$ and use the same g_χ normalization for all spin assignments; the different numerical prefactors in the partial widths below arise solely from the Lorentz structure of the current and spin/identical-particle statistics.

After electroweak symmetry breaking and diagonalization of the gauge-kinetic terms, the dominant low-energy interaction is $\varepsilon e A'_\mu J_{\text{EM}}^\mu$, up to $\mathcal{O}(m_U^2/m_Z^2)$ corrections from the induced Z -current coupling [15, 43].

The structure of the dark current J_χ^μ depends on the spin of the dark sector state and is given by [44]

$$J_\chi^\mu = \begin{cases} \bar{\chi} \gamma^\mu \chi, & \text{Dirac fermion,} \\ \frac{1}{2} \bar{\chi} \gamma^\mu \gamma^5 \chi, & \text{Majorana fermion,} \\ i(\varphi^\dagger \partial^\mu \varphi - (\partial^\mu \varphi^\dagger) \varphi), & \text{complex scalar,} \end{cases} \quad (2)$$

and the corresponding mass terms read

$$\mathcal{L}_{\text{mass}}^X = \begin{cases} -m_\chi \bar{\chi} \chi, & \text{Dirac fermion,} \\ -\frac{1}{2} m_\chi \bar{\chi} \chi, & \text{Majorana fermion,} \\ -m_\chi^2 \varphi^\dagger \varphi, & \text{complex scalar.} \end{cases} \quad (3)$$

Production of U from SM sources in hadronic and nuclear environments proceeds through kinetic mixing and therefore is universal at leading order, differing from the corresponding virtual-photon rate by an overall factor of ε^2 . Decays are controlled by the visible width into SM states and the invisible width into dark states. For charged leptons,

$$\Gamma(U \rightarrow \ell^+ \ell^-) = \frac{1}{3} \alpha \varepsilon^2 m_U \left(1 + \frac{2m_\ell^2}{m_U^2} \right) \sqrt{1 - \frac{4m_\ell^2}{m_U^2}}, \quad (4)$$

and the hadronic width is incorporated via the data-driven R -ratio (see Ref. [22, 38]),

$$\Gamma_{\text{had}}(m_U) = \Gamma_{\mu\mu}(m_U) R(m_U), \quad (5)$$

$$R(s) \equiv \left. \frac{\sigma(e^+ e^- \rightarrow \text{hadrons})}{\sigma(e^+ e^- \rightarrow \mu^+ \mu^-)} \right|_{s=m_U^2}. \quad (6)$$

The total visible width is obtained by summing all kinematically accessible SM final states,

$$\Gamma_{\text{vis}}(m_U) = \sum_{\ell=e,\mu,\tau} \Gamma(U \rightarrow \ell^+ \ell^-) + \Gamma_{\text{had}}, \quad (7)$$

and the branching ratio into electrons becomes

$$\text{Br}(U \rightarrow e^+ e^-) = \begin{cases} \frac{\Gamma(U \rightarrow e^+ e^-)}{\Gamma_{\text{vis}}}, & m_U < 2m_\chi, \\ \frac{\Gamma(U \rightarrow e^+ e^-)}{\Gamma_{\text{vis}} + \Gamma_{\text{inv}}}, & m_U \geq 2m_\chi, \end{cases} \quad (8)$$

where $\Gamma_{\text{inv}} = 0$ below threshold.

The invisible width Γ_{inv} depends on the Lorentz structure of the dark current and on the spectrum of dark

states. We consider three benchmark dark matter realizations:

(i) **Dirac fermion** χ with vector coupling $J_\chi^\mu = \bar{\chi}\gamma^\mu\chi$, for which

$$\Gamma(U \rightarrow \bar{\chi}\chi) = \frac{1}{3} \alpha_\chi m_U \left(1 + \frac{2m_\chi^2}{m_U^2}\right) \sqrt{1 - \frac{4m_\chi^2}{m_U^2}}. \quad (9)$$

(ii) **Majorana fermion** χ with axial-vector current $J_\chi^\mu = \bar{\chi}\gamma^\mu\gamma^5\chi$. Since the vector current vanishes identically for a Majorana field, the invisible width is

$$\Gamma(U \rightarrow \chi\chi) = \frac{1}{6} \alpha_\chi m_U \left(1 - \frac{4m_\chi^2}{m_U^2}\right)^{3/2}, \quad (10)$$

(iii) **Complex scalar** φ with current $J_\varphi^\mu = i\varphi^\dagger \overleftrightarrow{\partial}^\mu \varphi$, yielding [45]

$$\Gamma(U \rightarrow \varphi\varphi^\dagger) = \frac{1}{12} \alpha_\chi m_U \left(1 - \frac{4m_\chi^2}{m_U^2}\right)^{3/2}. \quad (11)$$

For Majorana dark matter the vector current vanishes identically, so the leading renormalizable interaction with a spin-1 mediator is axial. This yields the near-threshold scaling $\Gamma_{\text{inv}} \propto (1 - 4m_\chi^2/m_U^2)^{3/2}$ and the corresponding normalization in Eq. (10).

A. Visible and Invisible Decays of the Dark Photon

To illustrate how visible and invisible decay channels compete across the dark sector parameter space, Fig. 1 displays the dileptonic branching fraction $\text{Br}(U \rightarrow e^+e^-)$ in the (m_U, m_χ) plane for a fixed coupling $\alpha_\chi = 0.1$. The three panels correspond to the benchmark spin assignments considered throughout this work: Dirac fermion, Majorana fermion, and complex scalar dark matter.

The visible branching fraction is determined by the competition between the visible width $\Gamma_{\text{vis}}(m_U)$ and the invisible width $\Gamma_{\text{inv}}(m_U, m_\chi, \alpha_\chi)$, so that the transition between the *visible* and *invisible* regimes is controlled primarily by the kinematic opening of the dark channel at $m_U = 2m_\chi$.

Invisible regime ($m_U > 2m_\chi$). In each panel, a pronounced transition appears along the kinematic boundary $m_U = 2m_\chi$, where the invisible decay $U \rightarrow \chi\bar{\chi}$ (or $U \rightarrow XX^\dagger$ for scalar DM) becomes allowed and typically dominates the total width. Parametrically, close to threshold one has

$$\Gamma_{\text{inv}} \propto \alpha_\chi m_U \left(1 - \frac{4m_\chi^2}{m_U^2}\right)^p, \quad (12)$$

with $p = \frac{1}{2}$ for a Dirac fermion (unsuppressed *s*-wave phase space) and $p = \frac{3}{2}$ for Majorana and complex-scalar

final states (threshold suppression from the corresponding coupling/phase-space structure). As a result, once $m_U > 2m_\chi$ the visible branching fraction can drop by orders of magnitude, which is reflected in the steep decrease of $\text{Br}(U \rightarrow e^+e^-)$ to $\mathcal{O}(10^{-2})$ or below over large regions of parameter space.

Visible regime ($m_U < 2m_\chi$). For $m_U < 2m_\chi$ the dark channel is closed ($\Gamma_{\text{inv}} = 0$) and the dark photon decays exclusively into standard model states. In this region $\text{Br}(U \rightarrow e^+e^-)$ remains close to unity over most of the plane, with narrow modulations from QCD resonances. These features originate from the hadronic contribution to the total width, $\Gamma_{\text{had}}(m_U) \propto R(m_U) \Gamma_{\mu\mu}(m_U)$, which is enhanced near the ρ , ω , and ϕ poles and temporarily reduces the relative weight of the dilepton mode even in the absence of invisible decays.

The differences between the three spin scenarios are therefore driven mainly by the threshold behaviour of Γ_{inv} : Dirac dark matter, with an unsuppressed vector coupling, typically exhibits the most abrupt loss of visibility above threshold, while the Majorana and scalar cases display a somewhat smoother onset due to the stronger threshold suppression in Eq. (12). Overall, Fig. 1 identifies the regions in the (m_U, m_χ) plane where dilepton measurements are intrinsically most sensitive (visible regime) and those where invisible decays render the mediator effectively hidden, motivating complementary cosmological and astrophysical constraints.

Figure 2 provides a two-dimensional view of the decay pattern across the GeV mass range. The left panel corresponds to the visible regime, $m_U < 2m_\chi$, where phase space enforces the expected hierarchy of leptonic modes: $U \rightarrow e^+e^-$ dominates just above threshold, followed by $\mu^+\mu^-$ once $m_U > 2m_\mu$, and $\tau^+\tau^-$ for $m_U > 2m_\tau$. The hadronic contribution turns on near the two-pion threshold and exhibits pronounced resonance structure near the ρ , ω , and ϕ poles, which propagates directly into the leptonic branching fractions.

The right panel shows the invisible regime for a representative fermionic benchmark with $R = 3$ and $\alpha_\chi = 0.05$. Here $U \rightarrow \chi\bar{\chi}$ is open and typically dominates, so the invisible branching fraction stays close to unity except in narrow windows where hadronic resonances transiently enhance Γ_{vis} . Consequently, the standard model channels exhibit the same threshold and resonance pattern as in the visible case, but are globally suppressed by the large invisible width.

Having established how the dark photon decays into visible and invisible final states, we now turn to its production in the hot and dense environment created in relativistic nuclear collisions.

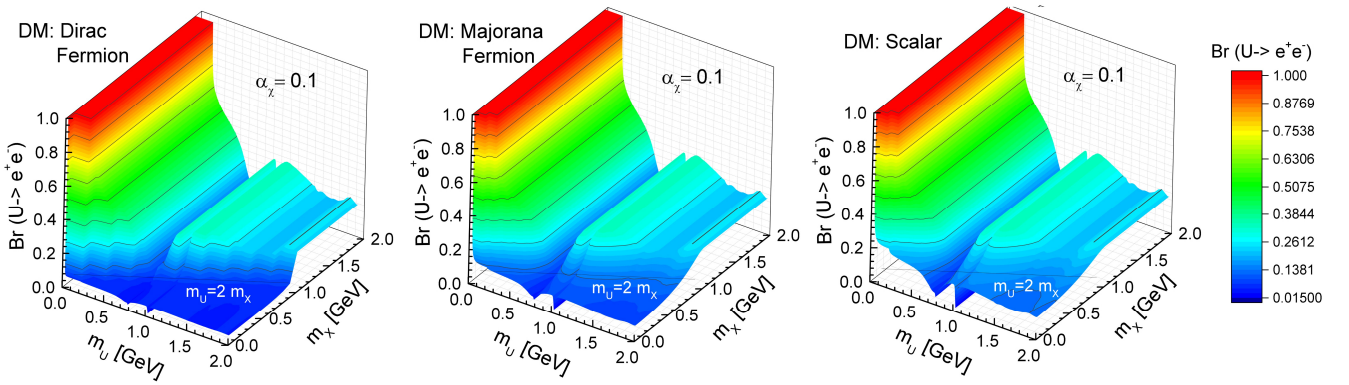


FIG. 1. Branching fraction $\text{Br}(U \rightarrow e^+ e^-)$ as a function of the mediator mass m_U and the dark matter mass m_χ for $\alpha_\chi = 0.1$, shown for three benchmark dark matter candidates: a Dirac fermion (left), a Majorana fermion (center), and a complex scalar (right). A sharp drop occurs along the kinematic threshold $m_U = 2m_\chi$, where the invisible decay $U \rightarrow \chi\bar{\chi}$ (or $U \rightarrow \varphi\varphi^\dagger$) opens and rapidly dominates the total width. Below threshold ($m_U < 2m_\chi$), decays proceed exclusively into standard model final states and the dileptonic branching fraction remains close to unity, modulated by hadronic contributions near the ρ , ω , and ϕ resonances. Differences among the three panels reflect the distinct spin structures and threshold behaviour of the invisible partial width Γ_{inv} for fermionic and scalar dark matter. The visible widths are taken from Ref. [46], while Γ_{inv} is computed from Eqs. (9)-(11).

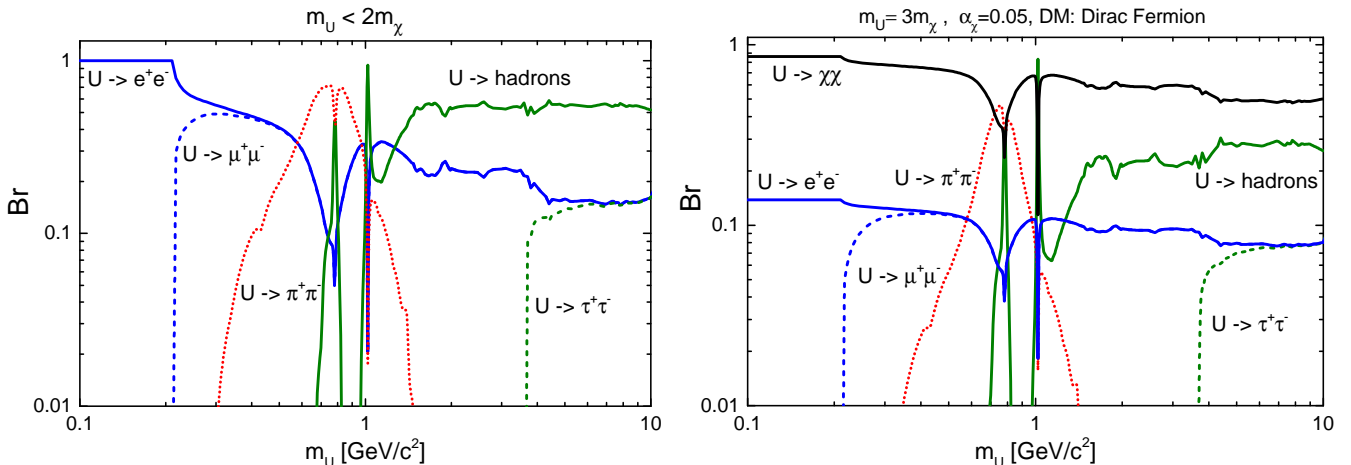


FIG. 2. Branching fractions of the dark photon U as a function of its mass m_U in the visible and invisible regimes. Left: *visible regime*, $m_U < 2m_\chi$, where decays into the dark sector are kinematically forbidden and the total width is shared among standard model final states. We show $U \rightarrow e^+ e^-$ (solid blue), $U \rightarrow \mu^+ \mu^-$ (dashed blue), $U \rightarrow \tau^+ \tau^-$ (dotted green), the inclusive hadronic mode (solid green), and the exclusive $\pi^+ \pi^-$ channel (dotted red). Right: *invisible regime* for fermionic dark matter, illustrated for $R \equiv m_U/m_\chi = 3$ and $\alpha_\chi = 0.05$. In this benchmark the invisible decay $U \rightarrow \chi\bar{\chi}$ (solid black) dominates over most of the mass range, while the standard model channels retain the same threshold and resonance structure as in the visible case but are globally suppressed. Prominent QCD resonances (ρ , ω , ϕ , ...) produce localized features in the hadronic curves and induce corresponding dips and peaks in the leptonic branching fractions. The visible (hadronic and leptonic) widths entering $\Gamma_{\text{vis}}(m_U)$ are taken from Ref. [46], while Γ_{inv} is computed from Eqs. (9)-(11).

III. STANDARD MATTER AND DARK PHOTON PRODUCTION IN PHSD

A. PHSD approach

The parton–hadron–string dynamics (PHSD) model is a microscopic, non–equilibrium transport approach that follows both hadronic and partonic degrees of freedom

throughout the full space–time evolution of a relativistic heavy-ion collision [47–52]. Starting from the first off-shell NN encounters, PHSD describes the string excitation and fragmentation, the formation and expansion of the quark–gluon plasma (QGP), the subsequent hadronization near the QCD cross-over, and the late hadronic rescattering and decays within a single unified framework.

The dynamics are obtained from the Cassing–Juchem off-shell transport equations, which arise from a first-order gradient expansion of the Kadanoff–Baym equations in test-particle representation and explicitly retain finite spectral functions [53, 54]. At high energy density, color strings melt into off-shell quarks, antiquarks and gluons described by the Dynamical Quasi-Particle Model (DQPM), whose complex self-energies and effective couplings are tuned to reproduce the lattice-QCD equation of state and transport coefficients over the (T, μ_B) plane [52, 55, 56]. As the system cools and dilutes, parton spectral functions sharpen and hadronization proceeds continuously; the ensuing hadronic system is then propagated with off-shell HSD dynamics. PHSD has been benchmarked from SIS to RHIC and LHC energies for a wide range of hadronic, photon, and dilepton observables (see, e.g., Refs. [51, 57] and the detailed discussion in Ref. [42]).

B. Dilepton production from standard model sources

Throughout the full evolution of the collision, PHSD tracks the emission of virtual photons, which subsequently convert into dilepton pairs. All established standard model sources are included as in Refs. [42, 51, 58]:

- *Low-mass hadronic channels ($M_{ee} \lesssim 1 \text{ GeV}/c^2$):* Dalitz decays of pseudoscalar mesons $\pi^0, \eta, \eta' \rightarrow \gamma e^+ e^-$ and baryon resonances $\Delta \rightarrow N e^+ e^-, N^* \rightarrow N e^+ e^-$, Dalitz transitions of vector and axial-vector mesons $\omega \rightarrow \pi^0 e^+ e^-, a_1 \rightarrow \pi e^+ e^-$, direct two-body decays of light vector mesons $\rho, \omega, \phi \rightarrow e^+ e^-$, as well as nucleon–nucleon and meson–nucleon bremsstrahlung $NN \rightarrow N N e^+ e^-$, $\pi N \rightarrow \pi N e^+ e^-$, all implemented with off-shell spectral functions and medium-modified widths as in Refs. [42, 51, 59, 60].
- *Partonic emission from the QGP:* annihilation and Compton-like processes $q\bar{q} \rightarrow \gamma^*, q\bar{q} \rightarrow g\gamma^*, qg(\bar{q}g) \rightarrow q(\bar{q})\gamma^*$, evaluated with DQPM propagators and a temperature- and density-dependent running coupling, thereby incorporating finite parton masses and widths, and reproducing the lattice-QCD equation of state [42, 52, 57].
- *Intermediate- and high-mass region:* correlated semileptonic decays of open-charm and open-beauty mesons (from $D\bar{D}, B\bar{B}$ production) dominate for $1 \lesssim M_{ee} \lesssim 3 \text{ GeV}/c^2$, with heavy-quark transport and energy loss treated as in Ref. [61]. At still higher masses, Drell–Yan-like $q\bar{q} \rightarrow \gamma^*$ processes in initial hard scatterings are included following the standard PHSD implementation [42, 51].

Radiation from hadronic resonances is implemented via the continuous “shining” procedure: each off-shell

resonance contributes to the dilepton yield along its trajectory according to its instantaneous electromagnetic width and local medium properties. This method consistently accounts for finite lifetimes, off-shell masses, and in-medium modifications of all emitters; a detailed description and validation are given in Refs. [42, 59, 60, 62].

C. Dark photon production in PHSD

Dark photon production is implemented as an extension of PHSD by introducing an on-shell dark photon U coupled through kinetic mixing and assuming a narrow width, such that each U contributes to a single invariant-mass bin in the dilepton spectrum [38, 39, 42].

We include the following production channels in PHSD:

$$\pi^0, \eta, \eta' \rightarrow \gamma U, \quad (13)$$

$$\omega \rightarrow \pi^0 U, \quad (14)$$

$$\Delta \rightarrow N U, \quad (15)$$

$$\rho, \omega, \phi \rightarrow U, \quad (16)$$

$$K^+ \rightarrow \pi^+ U, \quad (17)$$

$$q\bar{q} \rightarrow U. \quad (18)$$

For Dalitz-type channels $m \rightarrow \gamma U$ with $m = \pi^0, \eta, \eta'$ and for $\omega \rightarrow \pi^0 U$, we obtain the rates from the corresponding virtual-photon decays via the partial-width ratios $\Gamma_{m \rightarrow \gamma U}/\Gamma_{m \rightarrow \gamma\gamma}$ and $\Gamma_{\omega \rightarrow \pi^0 U}/\Gamma_{\omega \rightarrow \pi^0\gamma}$, which directly yield the $m \rightarrow XU$ branching ratios as in Refs. [20, 21, 63]. The $\Delta \rightarrow N U$ contribution is evaluated with the Δ spectral function and a mass-dependent total width following Refs. [22, 42, 60]. Direct decays of vector mesons $V = \rho, \omega, \phi$ are implemented by replacing the virtual photon by a dark photon with effective coupling $\alpha' = \alpha \varepsilon^2$ [20]. For the kaon mode $K^+ \rightarrow \pi^+ U$ we adopt the branching ratio from Ref. [64]. The partonic channel $q\bar{q} \rightarrow U$ is obtained by rescaling the PHSD $q\bar{q} \rightarrow \gamma^* \rightarrow e^+ e^-$ yield with ε^2 , exploiting the off-shell nature of DQPM partons which kinematically allows single- U production [42, 65].

Production from SM sources in hadronic and nuclear environments proceeds entirely through kinetic mixing and is therefore universal up to the overall factor ε^2 relative to the corresponding virtual-photon rate. The dilepton yield from dark photons then follows by multiplying the hadronic U yield by the visible branching fraction, while the partonic contribution is directly rescaled:

$$N_U = \sum_h N_{h \rightarrow UX} + N_{q\bar{q} \rightarrow U}, \quad (19)$$

$$N^{U \rightarrow e^+ e^-} = \text{Br}(U \rightarrow e^+ e^-) \sum_h N_{h \rightarrow UX} + \varepsilon^2 N_{q\bar{q} \rightarrow e^+ e^-}^{(M=m_U)}, \quad (20)$$

where h represents the sum over all hadronic sources (13–17). In Eq. (20) we treat hadronic and partonic

sources differently. For hadronic channels, PHSD produces on-shell dark photons U , and the observable dilepton yield is obtained by multiplying the produced U yield by the visible branching fraction $\text{Br}(U \rightarrow e^+ e^-)$. For the partonic contribution, we approximate on-shell U emission by mapping the PHSD virtual-photon yield from $q\bar{q} \rightarrow \gamma^* \rightarrow e^+ e^-$ at invariant mass $M = m_U$ onto $q\bar{q} \rightarrow U \rightarrow e^+ e^-$ in the narrow-width treatment; hence the final-state $e^+ e^-$ is already implicit, and the conversion amounts to a simple ε^2 rescaling of the corresponding γ^* yield.

For the partonic channel we implement U contribution by rescaling the corresponding virtual-photon dilepton yield at $M = m_U$ by ε^2 , which already yields the $e^+ e^-$ final state in the narrow-width treatment. A detailed derivation of the partial-width ratios, kinematic factors, and their numerical implementation in PHSD is provided in Ref. [42].

Rare channels such as $K^+ \rightarrow e^+ \nu U$, $\Sigma^+ \rightarrow p U$, or $D^{*0} \rightarrow D^0 U$, as well as production from primary Drell-Yan processes and electromagnetic bremsstrahlung, are not included, since their rates are either strongly constrained or subleading in the mass and energy ranges considered here (see, e.g., Refs. [25, 46, 64]).

With the dark photon production channels and the total dilepton yield Eq. (20), PHSD provides the dark photon contribution to the dilepton spectrum for any (m_U, ε) . We now use this prediction to convert the additional yield into quantitative upper limits on the kinetic mixing parameter $\varepsilon^2(M_U)$.

D. Extracting theoretical constraints on $\varepsilon^2(m_U)$

The kinetic mixing parameter ε^2 and the dark photon mass m_U are a priori free parameters.

Since PHSD provides the full invariant-mass spectrum from all SM sources, any additional contribution from dark photon production must appear only as a small perturbation of the SM yield.

For each invariant-mass bin of width dM (here $dM = 10$ MeV), we compute the integrated dark photon dilepton yield with m_U in $[m_U, m_U + dM]$ and divide by the bin width, defining

$$\frac{dN^{\text{sum}U}}{dM} = \sum_i \frac{N_i^{U \rightarrow e^+ e^-}}{dM}, \quad (21)$$

where the sum runs over all kinematically accessible production channels listed in Eqs. (13)-(18). Because each hadronic source scales as ε^2 and the partonic contribution is rescaled in the same way, the total yield is linear in ε^2 [42],

$$\frac{dN^{\text{sum}U}}{dM} = \varepsilon^2 \frac{dN_{\varepsilon=1}^{\text{sum}U}}{dM}, \quad (22)$$

where $dN_{\varepsilon=1}^{\text{sum}U}/dM$ is obtained by setting $\varepsilon = 1$ in the production amplitudes, while keeping the branching fractions (and hence the visible suppression in the invisible

regime) consistent with the chosen dark sector parameters.

To quantify the maximal dark photon contribution still compatible with the PHSD standard model (SM) dilepton yield in a given mass bin, we introduce a surplus factor C_U . The parameter C_U provides a measure of the excess over the PHSD SM yield, effectively capturing the combined experimental precision (see Refs. [38, 42] for more details). We require, in each mass bin,

$$\frac{dN^{\text{sum}U}}{dM} \leq C_U \frac{dN^{\text{sum}SM}}{dM}, \quad (23)$$

where $dN^{\text{sum}SM}/dM$ is the PHSD prediction from SM sources alone. Combining Eqs. (22) and (23) yields the bin-wise upper limit

$$\varepsilon^2 = C_U \left(\frac{dN^{\text{sum}SM}}{dM} \right) \left/ \left(\frac{dN_{\varepsilon=1}^{\text{sum}U}}{dM} \right) \right., \quad (24)$$

which we evaluate across the mediator-mass range of interest.

For presentation, it is convenient to distinguish the two limiting regimes:

$$\varepsilon^2 = \begin{cases} \varepsilon_{\text{vis}}^2(m_U), & m_U < 2m_\chi, \\ \varepsilon_{\text{inv}}^2(m_U, m_\chi, \alpha_\chi), & m_U > 2m_\chi, \end{cases} \quad (25)$$

where $\varepsilon_{\text{vis}}^2(m_U)$ corresponds to the peak search regime with $\text{Br}(U \rightarrow e^+ e^-) \simeq 1$, while $\varepsilon_{\text{inv}}^2(m_U, m_\chi, \alpha_\chi)$ accounts for the suppression of the dilepton signal through $\text{Br}(U \rightarrow e^+ e^-) \ll 1$ once $U \rightarrow \chi\bar{\chi}$ is open. Equation (24) makes explicit that the mapping between a bound on the dilepton excess and a bound on ε^2 depends on the dark sector parameters that control Γ_{inv} (e.g. α_χ and m_U/m_χ), as illustrated below.

Figure 3 summarizes the limits on the kinetic mixing parameter obtained from PHSD dilepton spectra in the visible and invisible regimes using Eq. 24. The left panel displays the visible bounds, $\varepsilon_{\text{vis}}^2(m_U)$, obtained under the assumption that the dark photon decays predominantly into standard model final states, in particular $U \rightarrow e^+ e^-$. In this regime, a dark photon would appear as a narrow peak above the SM dilepton spectra, so the extracted limits correspond to the maximal value of ε^2 for which the PHSD prediction remains consistent with the measured spectra. Exclusion bounds from fixed-target, collider, and beam-dump experiments have been added for comparison and shown as the hatched filled regions [25, 66]. A detailed discussion of the visible decay analysis and comparison with the experimental upper limits can be found in our previous work [42].

The right panel displays the invisible bounds, $\varepsilon_{\text{inv}}^2(m_U)$, obtained when the decay channel $U \rightarrow \chi\bar{\chi}$ is open and dominates the total width. The PHSD limits remain competitive across the sub-GeV mass range

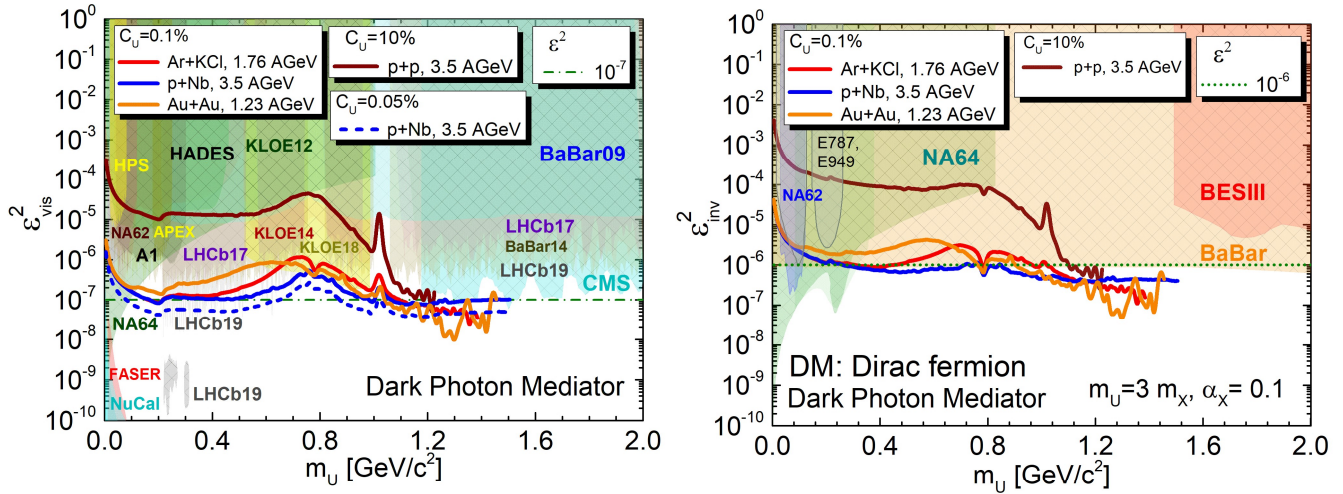


FIG. 3. Upper limits on the kinetic-mixing parameter for visible and invisible dark photon decays, $\varepsilon_{\text{vis}}^2(m_U)$ (left) and $\varepsilon_{\text{inv}}^2(m_U)$ (right), obtained from PHSD fits to dilepton spectra in $p + p$ at $E_{\text{lab}} = 3.5$ AGeV (brown), $Au + Au$ at $E_{\text{lab}} = 1.23$ AGeV (orange), $p + Nb$ at $E_{\text{lab}} = 3.5$ AGeV (blue), and $Ar + KCl$ at $E_{\text{lab}} = 1.76$ AGeV (red). We assume a Dirac fermion as the dark matter candidate for the invisible kinetic mixing. For comparison, the left panel includes existing exclusion limits from HADES, HPS, NA62, NA64, APEX, A1, KLOE, BaBar, LHCb, FASER, NuCal and CMS [25, 66], while the right panel shows the leading invisible search bounds from NA64, E787/E949, BaBar and BESIII [67–69]. Horizontal green lines indicate benchmark values $\varepsilon^2 = 10^{-7}$ (dot dashed) in the left panel, and $\varepsilon^2 = 10^{-6}$ (dotted) in the right panel. PHSD curves correspond to surplus parameters C_U as indicated in the legends: $C_U = 0.1\%$ for all systems, with additional curves for $C_U = 10\%$ in $p + p$ at $E_{\text{lab}} = 3.5$ AGeV (both panels) and $C_U = 0.05\%$ in $p + Nb$ at $E_{\text{lab}} = 3.5$ AGeV (left panel). A Dirac fermion has been used as a DM candidate.

and are shown together with leading invisible search constraints from NA64, E787/E949, BaBar, and BESIII [67–69].

Overall, the two panels highlight that dilepton measurements in heavy-ion and proton-nucleus collisions provide complementary sensitivity to visible and invisible dark photon scenarios. By covering mediator masses below and above hadronic resonances and by probing distinct decay regimes, the PHSD-based limits offer a unique contribution to the global dark photon parameter space.

Figure 4 extends the invisible constraints of Fig. 3 (right) by explicitly scanning the dark sector parameters α_χ and m_U/m_χ . For a fixed PHSD surplus $C_U = 0.1\%$, each coloured band encodes how the mapping from the visible PHSD yield to the underlying $\varepsilon_{\text{inv}}^2(m_U, m_\chi, \alpha_\chi)$ changes when the invisible width $\Gamma_{\text{inv}}(U \rightarrow \chi\bar{\chi})$ is modified.

The blue band illustrates the effect of varying the coupling $0.05 \leq \alpha_\chi \leq 0.5$ at fixed ratio $m_U = 3m_\chi$: increasing α_χ enhances Γ_{inv} , reduces the visible branching fraction Br_{vis} , and therefore requires a larger ε^2 to produce the same dilepton excess, pushing the upper edge of the band upward. The red and green bands, instead, keep α_χ fixed and bracket the range between $m_U/m_\chi = 2.1$ and 10. For given α_χ , lowering m_χ (larger m_U/m_χ) again strengthens the invisible channel and weakens the PHSD limit, while heavier dark matter leads to a smaller invisible width and correspondingly stronger bounds (lower parts of the bands).

The tightest limits are obtained for the benchmark with small coupling and heavy dark matter (green band, $\alpha_\chi = 0.05$, $m_U = 10m_\chi$), which approaches the level $\varepsilon^2 \sim 10^{-7}$ over a broad mass range. Because the PHSD yield scales linearly with the surplus parameter C_U , this curve can equivalently be interpreted as corresponding to an effective excess of $C_U \simeq 0.01\%$ over the SM baseline, rather than 0.1% as adopted in Fig. 3. This comparison illustrates both the sensitivity of heavy-ion dilepton data to invisible dark photon decays and the role played by the dark sector parameters in translating the PHSD bounds into constraints on the fundamental kinetic mixing.

In summary, the PHSD analysis provides upper limits on the kinetic mixing parameter ε^2 in both the visible and invisible regimes, for a range of dark sector benchmarks (m_χ, m_U, α_χ). These bounds, however, do not by themselves guarantee a viable dark matter scenario: the same mediator that controls the dark photon phenomenology also governs the self-scattering of dark matter in astrophysical halos. In the following section, we therefore turn to Self-Interacting Dark Matter (SIDM) and compute the velocity-dependent self-interaction cross section, in order to confront our benchmark models with astrophysical constraints from dwarf galaxies, galaxies, and clusters.

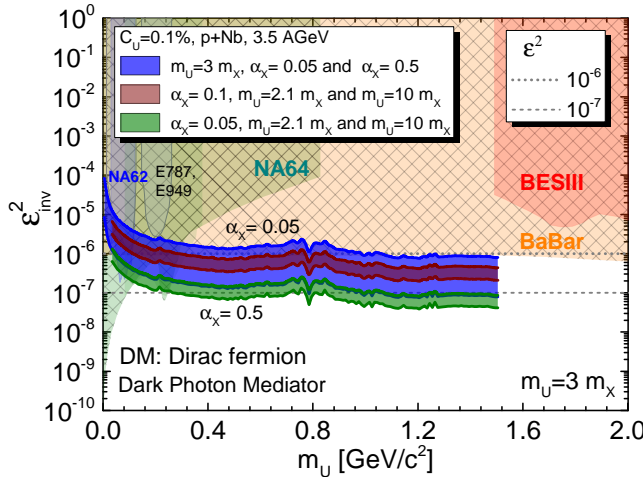


FIG. 4. Invisible decay constraints on the kinetic mixing parameter, $\varepsilon_{\text{inv}}^2(m_U, m_\chi, \alpha_\chi)$, obtained from PHSD for $p + Nb$ collisions at $E_{\text{lab}} = 3.5 \text{ AGeV}$ with surplus parameter $C_U = 0.1\%$, assuming a Dirac fermion as dark matter candidate. The vertical axis shows the upper limit on $\varepsilon_{\text{inv}}^2$ as a function of the mediator mass m_U , while the coloured bands illustrate the impact of varying the dark coupling α_χ and the mass ratio m_U/m_χ . The blue band corresponds to $m_U = 3m_\chi$ with α_χ varied between 0.05 and 0.5. The red band shows $\alpha_\chi = 0.1$ for two representative mass ratios, $m_U/m_\chi = 2.1$ and 10, and the green band displays the analogous variation for $\alpha_\chi = 0.05$. Existing invisible search bounds from NA62, NA64, E787/E949, BaBar, and BESIII [67–69] are shown as hatched filled regions. Horizontal grey lines indicate reference values $\varepsilon^2 = 10^{-6}$ (dotted) and 10^{-7} (dot-dashed).

IV. SELF-INTERACTING DARK MATTER

The standard Λ Cold Dark Matter (Λ CDM) paradigm, in which dark matter (DM) is cold and effectively collisionless, successfully accounts for large-scale cosmological observations, including the cosmic microwave background, galaxy clustering, and gravitational lensing [70]. On galactic and sub-galactic scales, however, several long-standing tensions between collisionless N -body predictions and inferred inner halo density profiles have been discussed. A prominent example is the core-cusp problem: while high-resolution simulations typically yield centrally steep profiles, $\rho(r) \propto r^{-1}$ [71], dwarf and low-surface-brightness galaxies often favor approximately constant-density cores in their inner regions [72].

Self-interacting dark matter (SIDM) provides a minimal and well-motivated extension of Λ CDM in which DM particles undergo elastic scattering with one another [73]. For cross sections per unit mass in the approximate range $\sigma/m_\chi \sim 0.1\text{--}10 \text{ cm}^2 \text{ g}^{-1}$, self-interactions enable efficient heat transport and partial thermalization of halo centers, thereby softening cusps into cores while leaving the large-scale successes of Λ CDM essentially unchanged.

A central requirement is that the interaction strength depends on the typical velocity scale of the system.

Dwarf galaxies probe relative velocities of order $\langle v \rangle \sim 50 \text{ km s}^{-1}$, where sizeable self-interactions can produce kiloparsec-scale cores, whereas Milky-Way- sized halos probe an intermediate regime, $\langle v \rangle \sim 250 \text{ km s}^{-1}$. At larger mass scales, galaxy groups and clusters reach substantially higher velocities, $\langle v \rangle \sim 1150\text{--}1900 \text{ km s}^{-1}$, and therefore impose stringent upper limits, since excessive scattering would noticeably alter their shapes and internal dynamics. Viable SIDM scenarios must therefore feature a pronounced suppression of σ/m_χ at group and cluster velocities while allowing comparatively large values at dwarf scales [74].

This scale dependence arises naturally if the self-interaction is mediated by a light force carrier: the resulting Yukawa potential yields a velocity-dependent transport cross section $\sigma(v)$ that decreases at high velocities [75]. In the remainder of this section we adopt this framework for a dark photon mediator and compute the relevant velocity-dependent self-interaction cross sections, enabling a direct comparison with astrophysical constraints from dwarfs, galaxies, groups, and clusters.

A. Calculations of self-interaction cross sections

In this work we compute the velocity-dependent transport cross sections with the public code CLASSICS (*CalcuLAtionS of Self-Interaction Cross Sections*) [74], which provides fast and accurate solutions of the non-relativistic scattering problem for Yukawa interactions, [7, 76],

$$V(r) = \pm \frac{\alpha_\chi}{r} e^{-m_U r}, \quad (26)$$

where the upper (lower) sign corresponds to repulsive (attractive) interactions between like charges.

For structure formation, the relevant transport quantities are the momentum-transfer and viscosity cross sections [7, 73, 77],

$$\sigma_T(v) = \int d\Omega (1 - \cos \theta) \frac{d\sigma}{d\Omega}, \quad (27)$$

$$\sigma_V(v) = \int d\Omega \sin^2 \theta \frac{d\sigma}{d\Omega}, \quad (28)$$

which suppress forward scattering and quantify the efficiency of momentum/heat transport in halos. Here v denotes the relative velocity of the two scattering particles in the center-of-mass frame, $v \equiv |\mathbf{v}_1 - \mathbf{v}_2|$, which is the appropriate non-relativistic variable controlling Yukawa scattering.

The code can also account for the exchange symmetry of identical particles by decomposing the scattering into even and odd partial waves. This symmetry decomposition is implemented for the viscosity cross section σ_V , whose $\sin^2 \theta$ weighting emphasizes large-angle scattering and reduces sensitivity to the forward region, facilitating a robust even/odd separation [74]. Concretely,

one defines $\sigma_V^{\text{even}}(v)$ and $\sigma_V^{\text{odd}}(v)$ from the partial-wave expansion of the underlying two-body scattering amplitude, restricting to even or odd orbital angular momenta, respectively. For unpolarized dark matter, the physical viscosity cross section is obtained by averaging over these symmetry channels, this leads to the combinations

$$\sigma_V^{\text{scalar}}(v) = \sigma_V^{\text{even}}(v), \quad (29)$$

$$\sigma_V^{\text{fermion}}(v) = \frac{3}{4} \sigma_V^{\text{odd}}(v) + \frac{1}{4} \sigma_V^{\text{even}}(v), \quad (30)$$

$$\sigma_V^{\text{vector}}(v) = \frac{1}{3} \sigma_V^{\text{odd}}(v) + \frac{2}{3} \sigma_V^{\text{even}}(v). \quad (31)$$

where the weights reflect the multiplicities of antisymmetric and symmetric spin configurations for $s = 1/2$ and $s = 1$ particles.

B. Galaxy and group/cluster constraints

Galaxy groups and clusters provide an important laboratory for testing SIDM in the high-velocity regime, $\langle v \rangle \sim 10^3 \text{ km s}^{-1}$, where self-interactions must be sufficiently suppressed so as not to overly modify the inner density structure and halo shapes of massive systems. In this context, the literature reports both (i) values inferred from core-size measurements in relaxed halos within a given dynamical modelling, and (ii) complementary constraints based on the requirement that self-interactions remain compatible with observed halo properties.

In this work we adopt the Jeans+lensing analysis of relaxed systems presented in Ref. [78] as a phenomenological high-velocity criterion at $\langle v \rangle \sim 10^3 \text{ km s}^{-1}$. That analysis infers the interaction strength required to reproduce the measured core sizes of groups and clusters. Expressed in terms of a momentum-transfer cross section per unit mass, galaxy groups are consistent with $\sigma/m_\chi \sim \mathcal{O}(0.1\text{-}1) \text{ cm}^2 \text{ g}^{-1}$ at $\langle v \rangle \sim 10^3 \text{ km s}^{-1}$, while clusters favour somewhat smaller values. Operationally, we treat these inferred values as a conservative high-velocity viability band: parameter points predicting significantly larger self-interactions at group/cluster velocities are discarded, while points within (or below) the inferred band are retained for the combined analysis.

Fig. 5 shows the velocity-weighted transport quantity $\langle \sigma v \rangle/m_\chi$ as a function of the characteristic mean relative velocity $\langle v \rangle$ for Yukawa-mediated SIDM with a dark-photon mediator. The theory curves are obtained with the CLASSICS code [74], which computes the velocity-dependent momentum-transfer cross section $\sigma(v) \equiv \sigma_T(v)$ for Yukawa scattering. To facilitate a direct comparison with the group/cluster inferences of Ref. [78], which are quoted in terms of a Maxwell-Boltzmann averaged transport cross section, we use the quantity $\langle \sigma v \rangle/m_\chi \equiv \bar{\sigma}/m_\chi \langle v \rangle$, where $\bar{\sigma}_T$ is defined following Appendix C of Ref. [74] as

$$\bar{\sigma}_T \equiv \frac{\langle \sigma_T(v) v^2 \rangle}{16\sqrt{2} v_0^2 / \sqrt{\pi}}, \quad (32)$$

with angular brackets denoting an average over the Maxwell-Boltzmann relative velocity distribution. The corresponding mean relative velocity is $\langle v \rangle = 4v_0/\sqrt{\pi}$.

For direct comparison, the blue and red points with error bars show the interaction strengths inferred for galaxy groups and clusters, respectively, from the Jeans+lensing analysis of Ref. [78]. The grey diagonal dotted lines indicate constant values of σ/m_χ , obtained by dividing $\langle \sigma v \rangle/m_\chi$ by $\langle v \rangle$. Finally, the orange band indicates the range $0.1 \lesssim \sigma/m_\chi \lesssim 10 \text{ cm}^2 \text{ g}^{-1}$ at dwarf-galaxy velocities that is typically required to alleviate the core-cusp problem.

In the left panel of Fig. 5 we consider Dirac-fermion dark matter and show CLASSICS predictions for three benchmark choices of $(m_U, m_\chi, \alpha_\chi)$ [74]. For each point, repulsive (solid) and attractive (dashed) potentials yield very similar behaviour at group/cluster velocities, where the scattering is already close to the Born-like regime. The curves pass through the group/cluster band near $\langle v \rangle \sim 10^3 \text{ km s}^{-1}$ while remaining at or below $\sigma/m_\chi \sim \mathcal{O}(1) \text{ cm}^2 \text{ g}^{-1}$, demonstrating consistency with high-velocity halo constraints. Extrapolating the same curves to lower velocities shows that the interaction strength naturally increases towards the dwarf-galaxy band, indicating that the same parameters can produce efficient self-interactions in small halos while remaining viable at cluster scales.

The right panel focuses on a single benchmark, $(m_\chi, m_U, \alpha_\chi) = (190 \text{ GeV}, 3 \text{ MeV}, 0.5)$, and compares scalar and fermionic dark matter. For both repulsive and attractive interactions, the scalar and fermion curves are nearly indistinguishable over the velocity range probed by groups and clusters, differing only at the $\mathcal{O}(1)$ level due to the distinct partial-wave decompositions. This illustrates that, for mediator masses and couplings favoured by our combined analysis, the high-velocity SIDM phenomenology is only weakly spin-dependent, while still allowing sizable self-interactions at dwarf scales.

C. Effective self-interaction cross section

Astrophysical systems over a wide range of masses and characteristic velocities constrain the strength of dark matter self-interactions. For a given halo population, these constraints are commonly expressed in terms of an effective transport cross section per unit mass, evaluated at a characteristic relative velocity $\langle v \rangle$ (see Sec. IV A). Dwarf and low-surface-brightness galaxies typically prefer $\sigma_{\text{eff}}/m_\chi \sim 0.1\text{-}10 \text{ cm}^2 \text{ g}^{-1}$ at $\langle v \rangle \sim 20\text{-}80 \text{ km s}^{-1}$ in order to form kiloparsec-scale cores, whereas galaxy groups and clusters predominantly provide upper limits, requiring $\sigma_{\text{eff}}/m_\chi \lesssim \mathcal{O}(1) \text{ cm}^2 \text{ g}^{-1}$ at $\langle v \rangle \sim 10^3 \text{ km s}^{-1}$ so as not to overly round their central density profiles. In Fig. 6 we represent these measurements as colored points in the $(\langle v \rangle, \sigma_{\text{eff}}/m_\chi)$ plane using the compilation of Ref. [79] together with the **Darkium** database. To connect with these

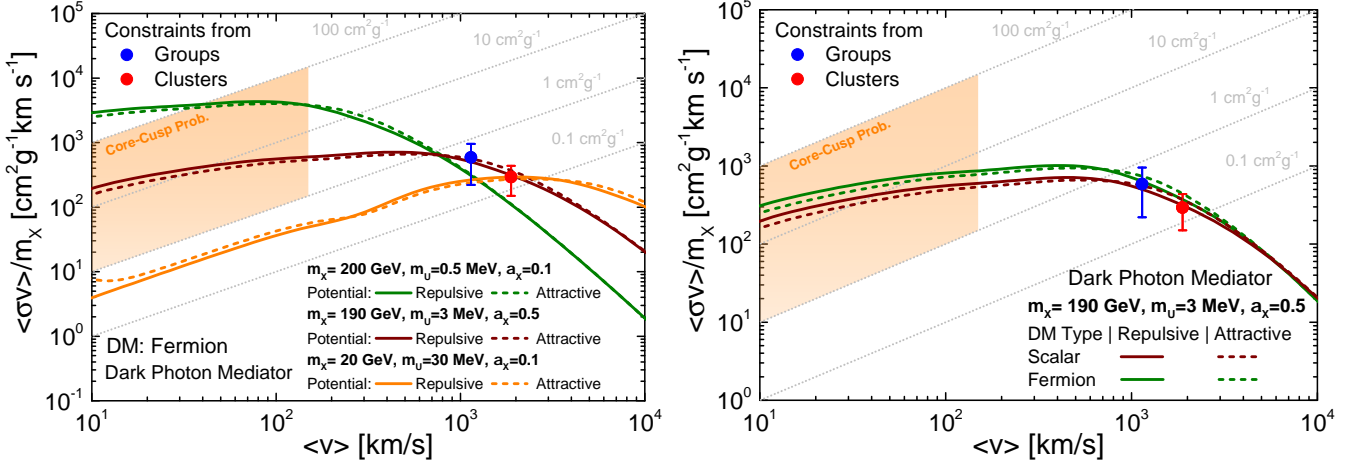


FIG. 5. Velocity-averaged momentum-transfer cross section per unit mass, $\langle\sigma v\rangle/m_\chi$, as a function of the mean relative velocity $\langle v \rangle$, for Yukawa-mediated SIDM with a dark-photon mediator. We added the group/cluster constraints taken from Ref. [78] for direct comparison. Grey diagonal dotted lines correspond to constant values of σ/m_χ multiplied by $\langle v \rangle$. Left: Dirac-fermion dark matter for three benchmark choices of $(m_\chi, m_U, \alpha_\chi)$ shown in the legend; solid (dashed) lines denote repulsive (attractive) interactions. Right: comparison between scalar and fermionic dark matter for the benchmark shown in the legend, again distinguishing repulsive (solid) and attractive (dashed) potentials. Blue and red points with error bars indicate the inferred interaction strengths for galaxy groups and clusters, respectively, as compiled in Ref. [78]; in our combined analysis these points are used as a high-velocity viability band, effectively excluding significantly larger cross sections at group/cluster velocities. Grey diagonal lines correspond to constant values of $\sigma/m_\chi = 0.1, 1, 10$ and $100 \text{ cm}^2 \text{ g}^{-1}$. The orange band marks the approximate range $0.1 \lesssim \sigma/m_\chi \lesssim 10 \text{ cm}^2 \text{ g}^{-1}$ at $\langle v \rangle \sim 10\text{-}200 \text{ km s}^{-1}$ that is typically required to alleviate the core-cusp problem in dwarf and low-surface-brightness galaxies. All theory curves are computed with CLASSICS [74].

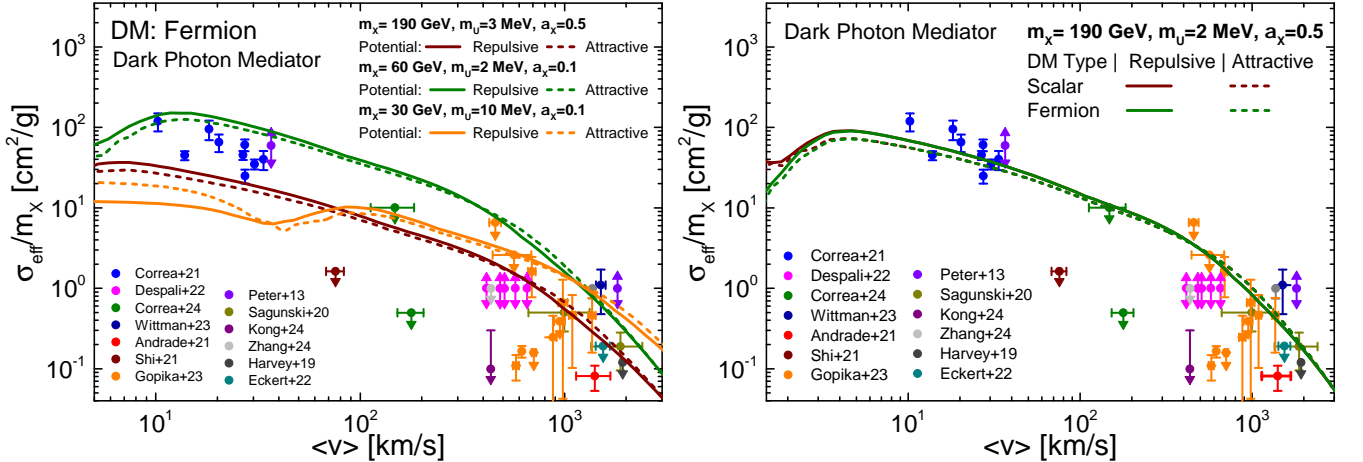


FIG. 6. Effective self-interaction cross section per unit mass, $\sigma_{\text{eff}}/m_\chi$, as a function of the mean relative velocity $\langle v \rangle$. The effective cross section σ_{eff} is constructed from the transfer-momentum cross section σ and the relative velocity distribution as defined in Eq. (33), making it a more direct proxy for halo heat transport than σ . Solid lines show theoretical predictions obtained with CLASSICS for Yukawa-mediated SIDM with a dark photon mediator. Left: Dirac-fermion dark matter for several benchmark choices of $(m_\chi, m_U, \alpha_\chi)$ indicated in the legend, for both repulsive (solid) and attractive (dashed) potentials. Right: comparison between scalar and fermionic dark matter for the fixed benchmark $(m_\chi, m_U, \alpha_\chi) = (190 \text{ GeV}, 2 \text{ MeV}, 0.5)$, again distinguishing repulsive (solid) and attractive (dashed) interactions. Colored points represent astrophysical estimates and bounds on $\sigma_{\text{eff}}/m_\chi$ from dwarf galaxies, Milky-Way-size halos, galaxy groups and clusters, compiled from Ref. [79] and the Darkium database.

constraints, we therefore use the definition of an effective

cross section [79],

$$\sigma_{\text{eff}} = \frac{3}{2} \frac{\langle \sigma(v) v^5 \rangle}{\langle v^5 \rangle}, \quad (33)$$

where angular brackets denote an average over the relative velocity distribution of the halo, which we approximate by a Maxwell-Boltzmann form. The v^5 weighting follows from kinetic-theory considerations in the long-mean-free-path regime and highlights the range of relative velocities that contributes most efficiently to heat transport. Here we construct σ_{eff} from the momentum-transfer cross section, $\sigma_T(v)$. When an even/odd partial-wave decomposition is needed for the spin averages discussed above, then we use the viscosity cross section $\sigma_V(v)$.

Figure 6 shows $\sigma_{\text{eff}}/m_\chi$ as a function of $\langle v \rangle$ for Yukawa-mediated SIDM with a dark photon mediator. In the left panel we consider Dirac fermion dark matter and display CLASSICS predictions for several benchmark choices of mediator mass m_U , dark matter mass m_χ , and coupling α_χ (see legend), for both repulsive (solid) and attractive (dashed) potentials. The velocity dependence reflects the transition from the nonperturbative regime at low velocities to the Born-like regime at high velocities: the interaction strength can reach $\sigma_{\text{eff}}/m_\chi \sim 0.1\text{-}10 \text{ cm}^2 \text{ g}^{-1}$ at dwarf velocities, while being suppressed at group/cluster velocities and remaining compatible with the corresponding upper limits.

The right panel focuses on the benchmark $(m_\chi, m_U, \alpha_\chi) = (190 \text{ GeV}, 2 \text{ MeV}, 0.5)$ and compares scalar and fermionic dark matter. Both spins exhibit a very similar velocity dependence, with modest normalization differences arising from the distinct partial-wave structure.

Overall, these results demonstrate that Yukawa-mediated SIDM models with $\alpha_\chi = \mathcal{O}(0.1\text{-}0.5)$ can simultaneously yield sizeable self-interactions at dwarf-galaxy velocities, as typically preferred by core data, while remaining consistent with the predominantly upper-limit constraints from galaxy groups and clusters.

V. THERMAL RELIC ABUNDANCE

The present-day abundance of a cold thermal relic is set by chemical freeze-out in the early Universe. For a dark matter species χ with mass m_χ and thermally averaged effective (co)annihilation rate $\langle \sigma_{\text{eff}} v \rangle$, it is convenient to work with the comoving number density $Y \equiv n_\chi/s$, where n_χ is the physical number density of χ and s is the entropy density. Introducing the dimensionless inverse temperature $x \equiv m_\chi/T$, with T the temperature of the thermal bath, the Boltzmann equation reads [10, 19, 80],

$$\frac{dY}{dx} = -\frac{s \langle \sigma_{\text{eff}} v \rangle}{H x} (Y^2 - Y_{\text{eq}}^2), \quad (34)$$

where $Y_{\text{eq}}(x) \equiv n_{\chi,\text{eq}}(T)/s(T)$ is the equilibrium yield. The entropy density is $s = (2\pi^2/45) g_{*s}(T) T^3$, with $g_{*s}(T)$ the effective number of relativistic degrees of freedom in entropy, and during radiation domination the Hubble rate is $H = \sqrt{4\pi^3 g_*(T)/45} T^2/M_{\text{Pl}}$, where $g_*(T)$

is the corresponding energy-density degrees of freedom and M_{Pl} denotes the (non-reduced) Planck mass. In the non-relativistic regime ($x \gg 1$), $Y_{\text{eq}} \propto x^{3/2} e^{-x}$, and freeze-out occurs once the annihilation rate per particle, $\Gamma_{\text{ann}} = n_\chi \langle \sigma_{\text{eff}} v \rangle$, drops below the Hubble expansion rate.

This formalism applies both to elastic and inelastic dark sectors. In general, $\langle \sigma_{\text{eff}} v \rangle$ denotes the thermally averaged effective rate controlling chemical decoupling, including the appropriate combination of annihilation and, when relevant, coannihilation channels, as well as any velocity dependence from thresholds and resonant effects in the underlying matrix elements.

Requiring the solution of the Boltzmann equation to reproduce the observed relic abundance, $\Omega_\chi h^2 \simeq 0.12$ [1, 9], selects a narrow band in parameter space. This band is often referred to as the thermal target. For conventional weakly coupled scenarios it corresponds to the well-known benchmark scale $\langle \sigma_{\text{eff}} v \rangle \sim \mathcal{O}(10^{-26}) \text{ cm}^3 \text{ s}^{-1}$, up to $\mathcal{O}(1)$ variations due to the particle-physics realization and the temperature dependence of $\langle \sigma_{\text{eff}} v \rangle$.

In the following, we determine the thermal target for the dark photon framework [11, 12, 44] considered in this work and confront them with laboratory constraints on the kinetic mixing, as well as with the astrophysical requirements implied by self-interacting dark matter.

A. Relic density calculation

To compute the thermal relic abundance in vector-mediated dark-sector scenarios, we employ the public RED-DELIVER code [81], which provides a self-consistent evaluation of the thermally averaged annihilation rate $\langle \sigma v \rangle(T)$ including mediator-width effects and the relevant Standard-Model thresholds. Mediator partial widths and branching ratios are implemented in a data-driven manner, ensuring that threshold openings, the transition from leptonic to hadronic channels, and resonance effects are consistently reflected in the thermal average.

In this work, we focus on elastic dark matter scenarios, corresponding to a single stable species coupled to the dark photon. We consider three representative realizations of the dark sector: (i) a Dirac fermion, (ii) a Majorana fermion, and (iii) a complex scalar. For the fermionic cases, the Majorana and Dirac limits are treated separately, while in all cases, the relic abundance is governed by standard $2 \rightarrow 2$ annihilation processes.

The dominant freeze-out channel is annihilation into Standard-Model fermions via an s -channel dark photon, $\chi \bar{\chi} \rightarrow f \bar{f}$ (or $\varphi^* \varphi \rightarrow f \bar{f}$ for scalar DM). In the non-relativistic limit, Dirac fermions typically admit an s -wave contribution, whereas complex scalars and Majorana DM are p -wave suppressed, $\sigma v \propto v^2$. This spin-dependent velocity scaling is automatically captured by the matrix elements implemented in RED-DELIVER.

The thermal evolution is described by a single Boltz-

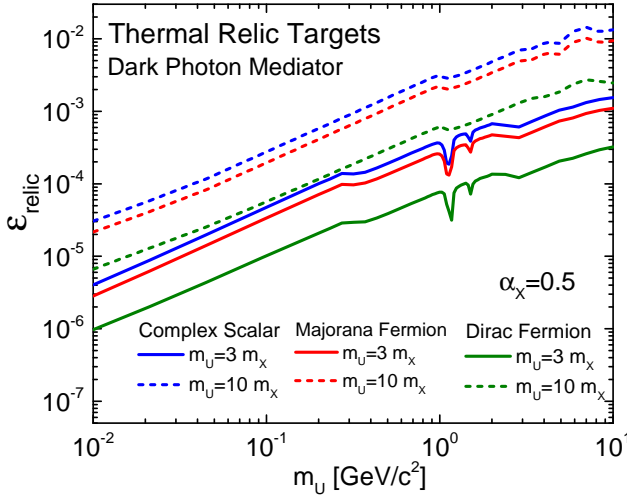


FIG. 7. Thermal relic target curves for the kinetic mixing parameter ε as a function of the mediator mass m_U at fixed dark coupling $\alpha_\chi = 0.5$, obtained with RED-DELiVER [81] by imposing the relic density condition $\Omega_\chi h^2 \simeq 0.12$. For each curve we fix the mass hierarchy $R \equiv m_U/m_\chi$, taking $R = 3$ (solid) and $R = 10$ (dashed), and scan m_U ; the dark matter mass varies along the curve as $m_\chi = m_U/R$. Colours denote the DM spin assignment: complex scalar (blue), Majorana fermion (red), and Dirac fermion (green). Localized dips arise from the interplay of hadronic thresholds in the mediator width and resonant s -channel enhancement near $m_U \simeq 2m_\chi$.

mann equation for the comoving abundance (Eq. 34), with an effective annihilation cross section $\langle\sigma v\rangle$ that fully incorporates mediator width effects and the velocity dependence induced by resonant annihilation near $m_U \simeq 2m_\chi$

For each point in the parameter space $(m_\chi, m_U, \varepsilon, g_\chi)$, RED-DELiVER solves the freeze-out dynamics and computes the relic density $\Omega_\chi h^2$. The corresponding thermal target curves, defined as the set of parameter points that reproduce the observed relic abundance, $\Omega_{\text{DM}} h^2 \simeq 0.12$, are used throughout this work as a reference to compare with constraints from heavy-ion collisions, accelerator and beam-dump experiments, as well as astrophysical limits from self-interacting dark matter.

Unless stated otherwise, each thermal relic curve shown below is obtained by fixing the dark coupling α_χ and a mass hierarchy $R \equiv m_U/m_\chi$, and then scanning the mediator mass m_U . Along such a curve, the dark matter mass therefore varies as $m_\chi = m_U/R$. Accordingly, each point on a given (m_U, ε) (or (m_U, ε^2)) target corresponds to a distinct pair (m_χ, m_U) linked by the chosen hierarchy R .

Figure 7 shows the thermal relic target lines in the (m_U, ε) plane for a fixed dark coupling $\alpha_\chi = 0.5$. For each dark matter spin assignment, complex scalar (blue), Majorana fermion (red), and Dirac fermion (green), we display two representative mass hierarchies, $R = m_U/m_\chi = 3$ (solid) and 10 (dashed). Each curve corresponds to the value of the kinetic mixing $\varepsilon(m_U)$ required

to reproduce the observed relic abundance $\Omega_\chi h^2 \simeq 0.12$, as computed with RED-DELiVER; for fixed R , scanning m_U implies $m_\chi = m_U/R$ along the target.

The overall rise of the curves with m_U reflects the fact that, for a heavier mediator, a larger mixing is needed to maintain the canonical annihilation rate. The relative ordering encodes the spin dependence of the annihilation kernel: for fixed m_U and R , Dirac fermions typically require the smallest ε , Majorana fermions an intermediate value, and complex scalars the largest coupling to achieve the same relic density. This pattern is expected since Dirac annihilation is typically dominated by an s -wave contribution, while Majorana and complex scalar annihilation are often p -wave suppressed; therefore, for the same mass scale, a p -wave scenario generally needs a slightly larger ε to reach $\Omega_\chi h^2 \simeq 0.12$ because the effective annihilation rate decreases roughly as $1/x$ as the Universe cools ($x \equiv m_\chi/T$). Narrow dips around $m_U \sim \mathcal{O}(1 \text{ GeV})$ arise from the combined effect of (i) hadronic thresholds entering the mediator width and (ii) resonant s -channel annihilation close to the kinematic condition $m_U \simeq 2m_\chi$. These thermal targets provide the benchmark against which we compare the PHSD limits on ε obtained from heavy-ion dilepton spectra in the visible and invisible regimes.

Figure 8 shows how the thermal relic targets in the invisible regime are constrained by existing bounds on the kinetic mixing. Each coloured line corresponds to the value of $\varepsilon_{\text{relic}}^2(m_U)$ required to reproduce the observed dark matter abundance for a fixed coupling $\alpha_\chi = 0.5$ and a fixed mass ratio $R = m_U/m_\chi$, for Dirac fermion DM (left) and complex scalar DM (right). Whenever a thermal relic curve enters one of the shaded exclusion regions from NA64, NA62, E787/E949, BaBar, or BE-SIII [67–69], the corresponding point in parameter space is ruled out: the model would require a kinetic mixing larger than experimentally allowed to achieve the correct relic density. Equivalently, these intersections map into excluded bands in the (m_χ, m_U) plane at fixed α_χ for each DM spin assignment, and only the segments of the thermal targets lying below all invisible limits are retained in our subsequent scans.

VI. $m_U(m_\chi)$ PARAMETER SPACE

Figure 9 summarizes our combined constraints in the (m_χ, m_U) plane for fermionic (left) and complex-scalar (right) dark matter interacting through a kinetically mixed dark photon. The different overlays encode, in a compact form, the interplay between (i) halo-scale self-interactions, (ii) early-Universe relic density targets, (iii) CMB limits at low masses, and (iv) heavy-ion bounds in the invisible regime.

The blue points indicate parameter choices for which the Yukawa-mediated self-interactions satisfy the effective self-interaction requirements compiled from dwarfs, Milky-Way-size halos, groups, and clusters, expressed in

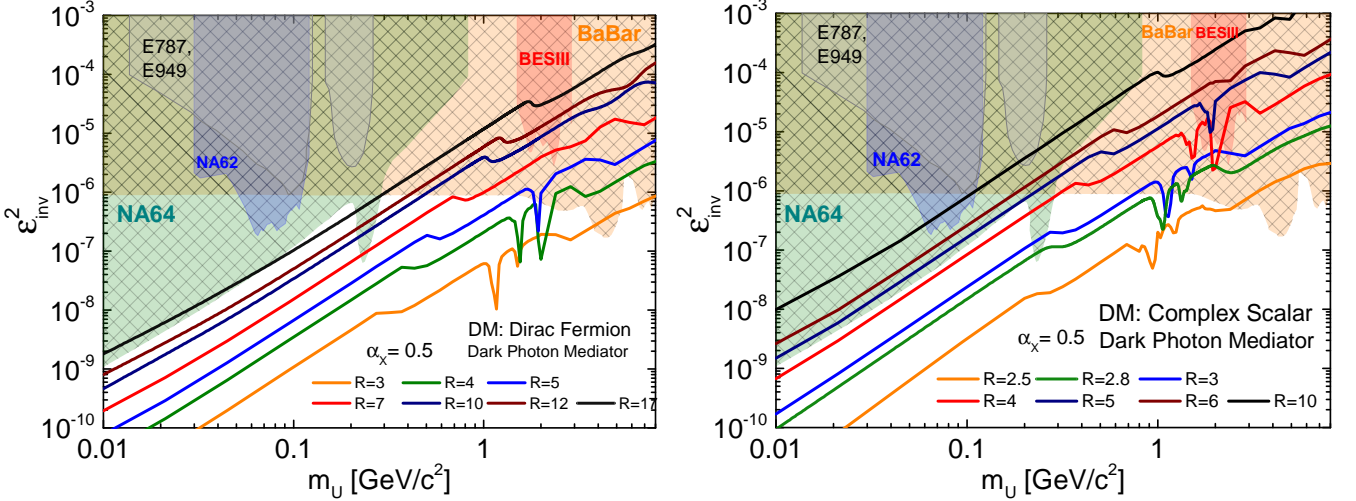


FIG. 8. Invisible search limits on the kinetic mixing parameter $\varepsilon_{\text{inv}}^2$ compared to thermal relic targets for a dark photon mediator. Shaded regions show existing constraints from NA64, NA62, E787/E949, BaBar, and BESIII in the $\varepsilon_{\text{inv}}^2$ - m_U plane. Solid curves are thermal relic targets computed with RED-DELIVER by imposing $\Omega_\chi h^2 \simeq 0.12$. In both panels we fix $\alpha_\chi = 0.5$ and, for each coloured line, fix the mass hierarchy $R \equiv m_U/m_\chi$ while scanning m_U ; equivalently, $m_\chi = m_U/R$ varies along the target. Left: Dirac-fermion DM targets for $R = 3, 4, 5, 7, 10, 12, 17$. Right: complex-scalar DM targets for $R = 2.5, 2.8, 3, 4, 5, 6, 10$. Localized dips arise from hadronic thresholds in the mediator width and from resonant s -channel enhancement near $m_U \simeq 2m_\chi$.

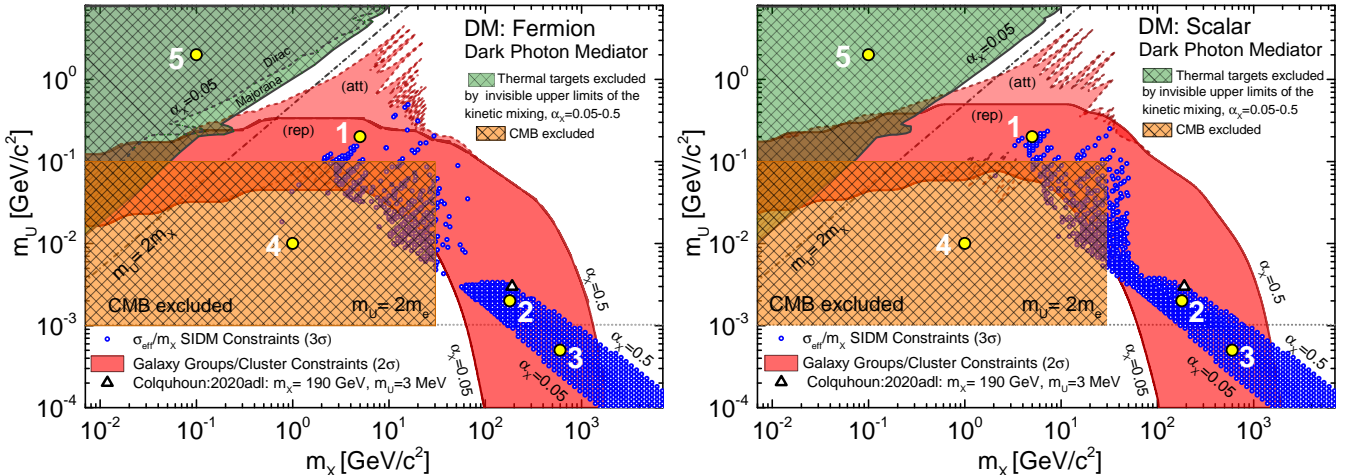


FIG. 9. Combined constraints in the (m_χ, m_U) plane for dark matter coupled to a dark photon mediator. Left: fermionic DM (Dirac or Majorana); right: complex scalar DM. Blue circles indicate parameter points where the Yukawa interaction reproduces the effective self-interaction cross-section constraints $\sigma_{\text{eff}}/m_\chi$ from dwarfs, galaxies, groups, and clusters (3σ), while the red band shows the subset consistent with the group/cluster constraints at 2σ . The orange hatched region at low masses is excluded by CMB data [1, 8], where dark matter radiation interactions would distort recombination and the CMB anisotropies. Green hatched regions mark thermal relic target points (for $\alpha_\chi = 0.05-0.5$) that are ruled out by the invisible upper limits on the kinetic mixing extracted from PHSD dilepton spectra. The diagonal line labelled $m_U = 2m_\chi$ denotes the kinematic threshold for $U \rightarrow \chi\bar{\chi}$, and the horizontal line at $m_U = 2m_e$ marks the opening of the e^+e^- channel. Dotted curves labelled $\alpha_\chi = 0.05$ and 0.5 illustrate typical coupling values, and the black triangle indicates the benchmark $m_\chi = 190$ GeV, $m_U = 3$ MeV of Ref. [74]. Five benchmark points (yellow circles): BP1-BP5 are highlighted in the figure and defined in the text.

terms of $\sigma_{\text{eff}}/m_\chi$ as described in Secs. IV A-IV C. These points yield sizeable interactions at dwarf velocities (supporting core formation) while remaining suppressed at group/cluster velocities, where the constraints are predominantly upper limits. The scan includes both signs

of the Yukawa potential, i.e. attractive and repulsive interactions.

The red band highlights the subset of blue points that additionally satisfies the group/cluster constraint at the 2σ level as implemented in Sec. IV B; operationally, it

delineates the high-velocity-viable portion of the SIDM parameter space used in our subsequent combined scans. Within this region, repulsive and attractive potentials are distinguished by dark and light red shading, respectively. As expected for attractive Yukawa scattering in the resonant/non-perturbative regime, the attractive case exhibits localized resonant enhancements, visible as narrow structures around $m_\chi \sim 1\text{-}20$ GeV and $m_U \sim 0.01\text{-}1$ GeV.

The orange hatched region at low (m_χ, m_U) is excluded by CMB constraints for $m_\chi \lesssim 30$ GeV and $1 \lesssim m_U \lesssim 100$ MeV (see Ref. [8] and also Refs. [1, 44, 82]). In this region, symmetric dark matter can still annihilate during recombination, $\chi\bar{\chi} \rightarrow UU$. Since the mediator decays mainly into electrons ($\text{Br}(U \rightarrow e^+e^-) \simeq 1$), it injects electromagnetic energy into the plasma. This alters the ionization history and is incompatible with the observed CMB anisotropies.

To project the heavy-ion constraints into the (m_χ, m_U) plane, we evaluate the PHSD upper limits on the kinetic mixing in the invisible regime, $\varepsilon_{\text{inv}}^2(m_U)$, and compare them to the kinetic mixing required to reproduce the observed relic abundance for each scanned point, $\varepsilon_{\text{relic}}^2(m_U, m_\chi, \alpha_\chi)$. The green hatched regions mark thermal relic parameter points for which $\Omega_{\text{DM}}h^2 \simeq 0.12$ is obtained (computed with RED-DELIVER for $\alpha_\chi = 0.05\text{-}0.5$), but which satisfy $\varepsilon_{\text{relic}}^2(m_U, m_\chi, \alpha_\chi) > \varepsilon_{\text{inv}}^2(m_U, m_\chi, \alpha_\chi)$ and are therefore excluded by the PHSD invisible limits. Equivalently, these regions indicate where a standard thermal history would predict an invisible decay scenario requiring kinetic mixing above the PHSD limit.

The diagonal dot-dashed line $m_U = 2m_\chi$ marks the kinematic threshold above which the mediator can decay invisibly to $\chi\bar{\chi}$, while the horizontal dotted line $m_U = 2m_e$ denotes the opening of the e^+e^- channel. The black triangle indicates the benchmark point $m_\chi = 190$ GeV, $m_U = 3$ MeV from Ref. [74].

To guide the discussion, we mark five benchmark points (BP1-BP5) in Fig. 9. BP1-BP3 are chosen inside the combined-allowed region to represent the three phenomenological regimes highlighted by our scan:

- 1. BP1: light mediator, intermediate DM.** A sub-GeV mediator with $m_U \simeq 0.2$ GeV and $m_\chi \simeq 5$ GeV. This point lies below the invisible threshold ($m_U < 2m_\chi$), so dilepton searches operate in the visible regime and production is dominated by hadronic sources (Dalitz decays, vector mesons, and baryon resonances), providing a clean target for precision low-mass spectra.
- 2. BP2: ultra-light mediator, heavy DM.** An MeV-scale mediator with $m_U \simeq 2$ MeV and $m_\chi \simeq 180$ GeV, representative of a strongly hierarchical Yukawa-mediated SIDM realization. In this setup, the self-interaction exhibits pronounced velocity dependence: it can be sizable at dwarf and group velocities while remaining sufficiently suppressed at cluster scales. This benchmark is compatible with both the group/cluster constraints (as in Ref. [74]) and the bounds based on the effective self-interaction cross section.
- 3. BP3: long-lived mediator, heavy DM.** A benchmark with a very light mediator, $m_U < 2m_e$, with $m_U \simeq 0.5$ MeV and $m_\chi \simeq 600$ GeV, for which all visible decays into charged SM states are kinematically forbidden and the invisible channel $U \rightarrow \chi\bar{\chi}$ is closed. Consequently, the mediator is effectively long-lived on detector scales; its phenomenology is governed by production via kinetic mixing and by loop-induced radiative decays (e.g. $U \rightarrow 3\gamma$), which are typically extremely suppressed in this mass range [83].
- 4. BP4: CMB-excluded point.** A representative low-mass configuration in the excluded domain (orange hatched), chosen at $m_\chi \simeq 1$ GeV and $m_U \simeq 10$ MeV. In this region, energy injection from residual annihilation around recombination can significantly modify the ionization history and hence the CMB temperature and polarization anisotropies, rendering this parameter point incompatible with CMB constraints.
- 5. BP5: PHSD-invisible excluded thermal point.** A representative thermal relic configuration in the green hatched region, chosen at $m_\chi \simeq 0.1$ GeV and $m_U \simeq 2$ GeV with $m_U > 2m_\chi$, such that invisible decays are kinematically allowed. For these masses, achieving $\Omega_{\text{DM}}h^2 \simeq 0.12$ within the scanned range $\alpha_\chi = 0.05\text{-}0.5$ requires a kinetic mixing ε^2 that exceeds the PHSD-derived invisible upper limits, rendering this point incompatible with the heavy-ion constraints.

Taken together, the two panels show that the simultaneous requirements of (i) efficient self-interactions at dwarf scales, (ii) suppression at group/cluster velocities, (iii) consistency with CMB bounds, and (iv) compatibility with the invisible heavy-ion limits substantially restrict the viable parameter space. In our scan, the permitted region is typically concentrated at light mediators in the MeV-sub-GeV range and comparatively heavy dark matter, from a few GeV up to the TeV scale. In this regime, Yukawa screening and the transition toward the Born (weak-coupling) limit suppress the interaction strength at high velocities while allowing enhanced scattering in small halos. Differences between the fermionic and scalar panels are driven primarily by the spin dependence of the annihilation kernel (and hence the thermal targets) and by the corresponding invisible widths, while the overall structure of the allowed region remains similar.

Altogether, our results indicate that the sub-threshold region $m_U < 2m_\chi$ is typically favored in the combined analysis, since the mediator cannot decay invisibly and, for $m_U > 2m_e$, remains directly visible in dileptons with an unsuppressed branching fraction. For $m_U > 2m_\chi$ invisible decays reduce $\text{Br}(U \rightarrow e^+e^-)$ and tighten the viable thermal relic parameter space once the invisible limits are applied, while the very light-mediator domain $m_U < 2m_e$ corresponds to a long-lived scenario that is not probed by the dilepton channel.

VII. SUMMARY

We have investigated a vector portal dark sector in which a kinetically mixed dark photon U couples to the standard model electromagnetic current with strength εe and to a stable, symmetric, and elastic dark sector particle through a dark gauge coupling g_χ (equivalently α_χ). This defines a parameter space $(m_U, \varepsilon, m_\chi, \alpha_\chi)$ that connects heavy-ion dilepton observables to thermal freeze-out and to velocity dependent self-interactions relevant for structure formation. We considered three benchmark realizations of the dark sector state: a Dirac fermion, a Majorana fermion (axial vector coupling), and a complex scalar.

On the high-energy collision side, we used the PHSD transport approach, including an on-shell dark photon produced from hadronic Dalitz channels, baryon-resonance transitions, direct vector-meson decays, kaon decays, and partonic $q\bar{q} \rightarrow U$ annihilation, followed by $U \rightarrow e^+e^-$ decays. Taking the PHSD standard model dilepton spectrum as a reference, we derived upper limits on the kinetic mixing, $\varepsilon^2(m_U)$ for the invisible regime ($m_U > 2m_\chi$), where $U \rightarrow \chi\bar{\chi}$ suppresses the dilepton branching fraction.

Furthermore, we incorporated cosmological and astrophysical requirements in two complementary ways. First, we computed Yukawa-mediated self-interaction cross sections using CLASSICS and constructed the effective transport quantity $\sigma_{\text{eff}}/m_\chi$ used throughout our halo level analysis. Confronting these predictions with compilations of constraints and inferences from dwarfs, Milky-Way-size halos, groups, and clusters, we identified regions in which self-interactions are sufficiently large at dwarf velocities to support core formation while remaining suppressed at group/cluster velocities. Second, we obtained thermal relic target curves with RED-DELIVER by imposing $\Omega_{\text{DM}}h^2 \simeq 0.12$, incorporating mediator width effects and hadronic thresholds.

Combining these ingredients, we mapped the viable parameter space in the (m_χ, m_U) plane for each DM spin assignment (Fig. 9). In the invisible regime, we project the

heavy-ion constraints by comparing the kinetic mixing required by freeze-out, $\varepsilon_{\text{relic}}^2(m_U, m_\chi, \alpha_\chi)$, to the invisible upper limits $\varepsilon_{\text{inv}}^2(m_U, m_\chi, \alpha_\chi)$, and we find that sizable portions of the would be thermal relic parameter space are already excluded. In addition, CMB bounds remove a broad low-mass region where energy injection around recombination would distort the measured anisotropies. The simultaneous requirement of SIDM-like scattering at dwarf scales and suppression at cluster scales further narrows the allowed region, typically favoring a light mediator in the MeV-sub-GeV range and heavier dark matter from a few tens of GeV up to the TeV scale.

To facilitate the interpretation of the combined constraints, we introduced five benchmark points (BP1-BP5) in Fig. 9. BP1-BP3 are chosen within the combined-allowed region and represent (i) a sub-GeV mediator with intermediate-mass DM in the visible regime, (ii) an ultra-light MeV mediator with heavy DM typical of hierarchical SIDM realizations, and (iii) a long-lived mediator scenario with $m_U < 2m_e$ and $m_U < 2m_\chi$, where both visible and invisible two-body decays are kinematically forbidden and only highly suppressed loop-induced channels remain. BP4 and BP5 are placed in excluded regions to illustrate, within the same plane, the impact of CMB exclusions at low masses and the removal of thermal relic points in the invisible regime by the PHSD $\varepsilon_{\text{inv}}^2(m_U)$ limits.

These findings favor the region $m_U < 2m_\chi$ with $m_U > 2m_e$, where the mediator remains visible in dileptons, while the very light-mediator domain $m_U < 2m_e$ corresponds to a long-lived scenario not directly probed by the dilepton channel. Taken together, precision dilepton measurements in heavy-ion collisions provide a complementary and competitive probe of vector-portal dark sectors when interpreted jointly with thermal freeze-out and SIDM phenomenology. Future improvements in low-mass dilepton data, extended system/energy coverage, and refined astrophysical inferences will further sharpen the combined constraints and help prioritize the most promising regions for experimental searches.

ACKNOWLEDGMENTS

A.R.J. expresses gratitude for the financial support from the Stiftung Giersch. We also acknowledge the support by the Deutsche Forschungsgemeinschaft (DFG) through the grant CRC-TR 211 "Strong-interaction matter under extreme conditions" (Project number 315477589 - TRR 211) and the CNRS Helmholtz Dark Matter Lab (DMLab). The computational resources utilized for this work were provided by the Center for Scientific Computing (CSC) at Goethe University Frankfurt.

[1] N. Aghanim *et al.* (Planck), Planck 2018 results. VI. Cosmological parameters, *Astron. Astrophys.* **641**, A6

(2020), [Erratum: *Astron. Astrophys.* 652, C4 (2021)],

arXiv:1807.06209 [astro-ph.CO].

[2] J. L. Feng, Dark Matter Candidates from Particle Physics and Methods of Detection, *Ann. Rev. Astron. Astrophys.* **48**, 495 (2010), arXiv:1003.0904 [astro-ph.CO].

[3] P. F. de Salas, K. Malhan, K. Freese, K. Hattori, and M. Valluri, On the estimation of the Local Dark Matter Density using the rotation curve of the Milky Way, *JCAP* **10**, 037, arXiv:1906.06133 [astro-ph.GA].

[4] D. Clowe, M. Bradac, A. H. Gonzalez, M. Markevitch, S. W. Randall, C. Jones, and D. Zaritsky, A direct empirical proof of the existence of dark matter, *Astrophys. J. Lett.* **648**, L109 (2006), arXiv:astro-ph/0608407.

[5] A. Mahdavi, H. y. Hoekstra, A. y. Babul, D. y. Balam, and P. Capak, A Dark Core in Abell 520, *Astrophys. J.* **668**, 806 (2007), arXiv:0706.3048 [astro-ph].

[6] J. S. Bullock and M. Boylan-Kolchin, Small-Scale Challenges to the Λ CDM Paradigm, *Ann. Rev. Astron. Astrophys.* **55**, 343 (2017), arXiv:1707.04256 [astro-ph.CO].

[7] S. Tulin and H.-B. Yu, Dark Matter Self-interactions and Small Scale Structure, *Phys. Rept.* **730**, 1 (2018), arXiv:1705.02358 [hep-ph].

[8] M. Kaplinghat, S. Tulin, and H.-B. Yu, Direct Detection Portals for Self-interacting Dark Matter, *Phys. Rev. D* **89**, 035009 (2014), arXiv:1310.7945 [hep-ph].

[9] G. Hinshaw *et al.* (WMAP), Nine-Year Wilkinson Microwave Anisotropy Probe (WMAP) Observations: Cosmological Parameter Results, *Astrophys. J. Suppl.* **208**, 19 (2013), arXiv:1212.5226 [astro-ph.CO].

[10] E. W. Kolb and M. S. Turner, *The Early Universe*, Vol. 69 (Taylor and Francis, 2019).

[11] J. Alexander *et al.*, Dark Sectors 2016 Workshop: Community Report, (2016).

[12] M. Battaglieri *et al.*, US Cosmic Visions: New Ideas in Dark Matter 2017: Community Report, in *U.S. Cosmic Visions: New Ideas in Dark Matter* (2017) arXiv:1707.04591 [hep-ph].

[13] P. Agrawal *et al.*, Feebly-interacting particles: FIPs 2020 workshop report, *Eur. Phys. J. C* **81**, 1015 (2021), arXiv:2102.12143 [hep-ph].

[14] G.-W. Yuan, Z.-Q. Shen, Y.-L. S. Tsai, Q. Yuan, and Y.-Z. Fan, Constraining ultralight bosonic dark matter with Keck observations of S2's orbit and kinematics, *Phys. Rev. D* **106**, 103024 (2022), arXiv:2205.04970 [astro-ph.HE].

[15] B. Holdom, Two U(1)'s and Epsilon Charge Shifts, *Phys. Lett. B* **166**, 196 (1986).

[16] P. Fayet, Effects of the Spin 1 Partner of the Goldstino (Gravitino) on Neutral Current Phenomenology, *Phys. Lett. B* **95**, 285 (1980).

[17] P. Fayet, Light spin 1/2 or spin 0 dark matter particles, *Phys. Rev. D* **70**, 023514 (2004), arXiv:hep-ph/0403226.

[18] C. Boehm and P. Fayet, Scalar dark matter candidates, *Nucl. Phys. B* **683**, 219 (2004), arXiv:hep-ph/0305261.

[19] M. Pospelov, A. Ritz, and M. B. Voloshin, Secluded WIMP Dark Matter, *Phys. Lett. B* **662**, 53 (2008), arXiv:0711.4866 [hep-ph].

[20] B. Batell, M. Pospelov, and A. Ritz, Exploring Portals to a Hidden Sector Through Fixed Targets, *Phys. Rev. D* **80**, 095024 (2009), arXiv:0906.5614 [hep-ph].

[21] B. Batell, M. Pospelov, and A. Ritz, Probing a Secluded U(1) at B-factories, *Phys. Rev. D* **79**, 115008 (2009), arXiv:0903.0363 [hep-ph].

[22] G. Agakishiev *et al.* (NA48/2), Search for a New Gauge Boson in Electron-Nucleus Fixed-Target Scattering by the NA48/2 Experiment, *Phys. Rev. Lett.* **107**, 191804 (2011), arXiv:1108.2750 [hep-ex].

[23] J. Beacham *et al.*, Physics Beyond Colliders at CERN: Beyond the Standard Model Working Group Report, *J. Phys. G* **47**, 010501 (2020), arXiv:1901.09966 [hep-ex].

[24] J. Billard *et al.*, Direct detection of dark matter—APPEC committee report*, *Rept. Prog. Phys.* **85**, 056201 (2022), arXiv:2104.07634 [hep-ex].

[25] M. Fabbrichesi, E. Gabrielli, and G. Lanfranchi, The physics of the dark photon, *SpringerBriefs in Physics* 10.1007/978-3-030-62519-1 (2021).

[26] S. Abrahamyan *et al.* (APEX), Search for a New Gauge Boson in Electron-Nucleus Fixed-Target Scattering by the APEX Experiment, *Phys. Rev. Lett.* **107**, 191804 (2011), arXiv:1108.2750 [hep-ex].

[27] P. H. Adrian *et al.* (HPS), Search for a dark photon in electroproduced e^+e^- pairs with the Heavy Photon Search experiment at JLab, *Phys. Rev. D* **98**, 091101 (2018), arXiv:1807.11530 [hep-ex].

[28] H. Merkel *et al.*, Search at the Mainz Microtron for Light Massive Gauge Bosons Relevant for the Muon g-2 Anomaly, *Phys. Rev. Lett.* **112**, 221802 (2014), arXiv:1404.5502 [hep-ex].

[29] J. R. Batley *et al.* (NA48/2), Search for the dark photon in π^0 decays, *Phys. Lett. B* **746**, 178 (2015), arXiv:1504.00607 [hep-ex].

[30] B. Aubert *et al.* (BaBar), Search for Dimuon Decays of a Light Scalar Boson in Radiative Transitions Upsilon \rightarrow gamma A0, *Phys. Rev. Lett.* **103**, 081803 (2009), arXiv:0905.4539 [hep-ex].

[31] J. P. Lees *et al.* (BaBar), Search for a Dark Photon in e^+e^- Collisions at BaBar, *Phys. Rev. Lett.* **113**, 201801 (2014), arXiv:1406.2980 [hep-ex].

[32] D. Babusci *et al.* (KLOE-2), Search for light vector boson production in $e^+e^- \rightarrow \mu^+\mu^-\gamma$ interactions with the KLOE experiment, *Phys. Lett. B* **736**, 459 (2014), arXiv:1404.7772 [hep-ex].

[33] D. Babusci *et al.* (KLOE-2), Limit on the production of a light vector gauge boson in phi meson decays with the KLOE detector, *Phys. Lett. B* **720**, 111 (2013), arXiv:1210.3927 [hep-ex].

[34] A. Anastasi *et al.* (KLOE-2), Combined limit on the production of a light gauge boson decaying into $\mu^+\mu^-$ and $\pi^+\pi^-$, *Phys. Lett. B* **784**, 336 (2018), arXiv:1807.02691 [hep-ex].

[35] R. Aaij *et al.* (LHCb), Search for Dark Photons Produced in 13 TeV pp Collisions, *Phys. Rev. Lett.* **120**, 061801 (2018), arXiv:1710.02867 [hep-ex].

[36] R. Aaij *et al.* (LHCb), Search for $A' \rightarrow \mu^+\mu^-$ decays, (2019), arXiv:1910.06926 [hep-ex].

[37] A. Hayrapetyan *et al.* (CMS), Search for direct production of GeV-scale resonances decaying to a pair of muons in proton-proton collisions at $\sqrt{s} = 13$ TeV, *JHEP* **12**, 070, arXiv:2309.16003 [hep-ex].

[38] I. Schmidt, E. Bratkovskaya, M. Gumberidze, and R. Holzmann, Constraints on the kinetic mixing parameter $\varepsilon 2$ for the light dark photons from dilepton production in heavy-ion collisions in the few-GeV energy range, *Phys. Rev. D* **104**, 015008 (2021), arXiv:2105.00569 [hep-ph].

[39] E. Bratkovskaya, I. Schmidt, M. Gumberidze, and R. Holzmann, Search for dark photons in heavy-ion collisions, *Astron. Nachr.* **344**, e220104 (2023).

[40] A. W. Romero Jorge, E. Bratkovskaya, and L. Sagunski, Search for dark photons in heavy-ion collisions, PoS

ICHEP2024, 290 (2025), arXiv:2409.20141 [hep-ph].

[41] A. W. R. Jorge, E. Bratkovskaya, T. Song, and L. Sagunski, Exploring Dark Photon Production and Kinetic Mixing Constraints in Heavy-Ion Collisions, *Astron. Nachr.* **346**, e20240132 (2025), arXiv:2412.02536 [hep-ph].

[42] A. W. R. Jorge, E. Bratkovskaya, T. Song, and L. Sagunski, Constraints on kinetic mixing of dark photons from dilepton spectra, *Phys. Rev. C* **112**, 054905 (2025), arXiv:2507.11163 [hep-ph].

[43] R. Essig *et al.*, Working Group Report: New Light Weakly Coupled Particles, in *Snowmass 2013: Snowmass on the Mississippi* (2013) arXiv:1311.0029 [hep-ph].

[44] G. Krnjaic, Testing Thermal-Relic Dark Matter with a Dark Photon Mediator, (2025), arXiv:2505.04626 [hep-ph].

[45] For notational simplicity we denote the dark matter mass by m_χ throughout, also in the complex-scalar case φ , i.e. $m_\varphi \equiv m_\chi$.

[46] P. Ilten, J. Thaler, M. Williams, and W. Xue, Dark photons from charm mesons at LHCb, *Phys. Rev. D* **92**, 115017 (2015), arXiv:1509.06765 [hep-ph].

[47] W. Cassing and E. L. Bratkovskaya, Parton transport and hadronization from the dynamical quasiparticle point of view, *Phys. Rev. C* **78**, 034919 (2008), arXiv:0808.0022 [hep-ph].

[48] W. Cassing, From Kadanoff-Baym dynamics to off-shell parton transport, *Eur. Phys. J. ST* **168**, 3 (2009), arXiv:0808.0715 [nucl-th].

[49] W. Cassing and E. L. Bratkovskaya, Parton-Hadron-String Dynamics: an off-shell transport approach for relativistic energies, *Nucl. Phys. A* **831**, 215 (2009), arXiv:0907.5331 [nucl-th].

[50] E. L. Bratkovskaya, W. Cassing, V. P. Konchakovski, and O. Linnyk, Parton-Hadron-String Dynamics at Relativistic Collider Energies, *Nucl. Phys. A* **856**, 162 (2011), arXiv:1101.5793 [nucl-th].

[51] O. Linnyk, E. L. Bratkovskaya, and W. Cassing, Effective QCD and transport description of dilepton and photon production in heavy-ion collisions and elementary processes, *Prog. Part. Nucl. Phys.* **87**, 50 (2016), arXiv:1512.08126 [nucl-th].

[52] P. Moreau, O. Soloveva, L. Oliva, T. Song, W. Cassing, and E. Bratkovskaya, Exploring the partonic phase at finite chemical potential within an extended off-shell transport approach, *Phys. Rev. C* **100**, 014911 (2019), arXiv:1903.10257 [nucl-th].

[53] W. Cassing and S. Juchem, Semiclassical transport of particles with dynamical spectral functions, *Nucl. Phys. A* **665**, 377 (2000), arXiv:nucl-th/9903070.

[54] S. Juchem, W. Cassing, and C. Greiner, Nonequilibrium quantum field dynamics and off-shell transport for ϕ^4 theory in (2+1)-dimensions, *Nucl. Phys. A* **743**, 92 (2004), arXiv:nucl-th/0401046.

[55] W. Cassing, QCD thermodynamics and confinement from a dynamical quasiparticle point of view, *Nucl. Phys. A* **791**, 365 (2007), arXiv:0704.1410 [nucl-th].

[56] O. Soloveva, P. Moreau, and E. Bratkovskaya, Transport coefficients for the hot quark-gluon plasma at finite chemical potential μ_B , *Phys. Rev. C* **101**, 045203 (2020), arXiv:1911.08547 [nucl-th].

[57] P. Moreau, O. Soloveva, I. Grishmanovskii, V. Voronyuk, L. Oliva, T. Song, V. Kireyeu, G. Coci, and E. Bratkovskaya, Properties of the quark-gluon plasma created in heavy-ion collisions, *Astron. Nachr.* **342**, 715 (2021), arXiv:2101.05688 [nucl-th].

[58] R. Rapp, Dilepton Spectroscopy of QCD Matter at Collider Energies, *Adv. High Energy Phys.* **2013**, 148253 (2013), arXiv:1304.2309 [hep-ph].

[59] E. L. Bratkovskaya and W. Cassing, Dilepton production and off-shell transport dynamics at SIS energies, *Nucl. Phys. A* **807**, 214 (2008), arXiv:0712.0635 [nucl-th].

[60] E. L. Bratkovskaya, J. Aichelin, M. Thomere, S. Vogel, and M. Bleicher, System size and energy dependence of dilepton production in heavy-ion collisions at 1-2 GeV/nucleon energies, *Phys. Rev. C* **87**, 064907 (2013), arXiv:1301.0786 [nucl-th].

[61] T. Song, W. Cassing, P. Moreau, and E. Bratkovskaya, Open charm and dileptons from relativistic heavy-ion collisions, *Phys. Rev. C* **97**, 064907 (2018), arXiv:1803.02698 [nucl-th].

[62] T. Galatyuk, P. M. Hohler, R. Rapp, F. Seck, and J. Stroth, Thermal Dileptons from Coarse-Grained Transport as Fireball Probes at SIS Energies, *Eur. Phys. J. A* **52**, 131 (2016), arXiv:1512.08688 [nucl-th].

[63] D. Gorbunov and D. Kalashnikov, NICA prospects in searches for light exotics from hidden sectors: The cases of hidden photons and axion-like particles, *Phys. Lett. B* **852**, 138599 (2024), arXiv:2401.12893 [hep-ph].

[64] M. Pospelov, Secluded U(1) below the weak scale, *Phys. Rev. D* **80**, 095002 (2009), arXiv:0811.1030 [hep-ph].

[65] A. Berlin, S. Gori, P. Schuster, and N. Toro, Dark Sectors at the Fermilab SeaQuest Experiment, *Phys. Rev. D* **98**, 035011 (2018), arXiv:1804.00661 [hep-ph].

[66] P. Ilten, Y. Soreq, M. Williams, and W. Xue, Serendipity in dark photon searches, *JHEP* **06**, 004, arXiv:1801.04847 [hep-ph].

[67] J. P. Lees *et al.* (BaBar), Search for Invisible Decays of a Dark Photon Produced in e^+e^- Collisions at BaBar, *Phys. Rev. Lett.* **119**, 131804 (2017), arXiv:1702.03327 [hep-ex].

[68] M. Ablikim *et al.* (BESIII), Search for invisible decays of a dark photon using e^+e^- annihilation data at BESIII, *Phys. Lett. B* **839**, 137785 (2023), arXiv:2209.13893 [hep-ex].

[69] P. Crivelli, Status and prospects of the NA64 experiment at the CERN SPS, in *Workshop on Feebly-Interacting Particles* (2023) arXiv:2301.09905 [hep-ex].

[70] C. S. Frenk and S. D. M. White, Dark matter and cosmic structure, *Annalen Phys.* **524**, 507 (2012), arXiv:1210.0544 [astro-ph.CO].

[71] J. F. Navarro, C. S. Frenk, and S. D. M. White, A Universal density profile from hierarchical clustering, *Astrophys. J.* **490**, 493 (1997), arXiv:astro-ph/9611107.

[72] W. J. G. de Blok, The Core-Cusp Problem, *Adv. Astron.* **2010**, 789293 (2010), arXiv:0910.3538 [astro-ph.CO].

[73] S. Tulin, H.-B. Yu, and K. M. Zurek, Beyond Collisionless Dark Matter: Particle Physics Dynamics for Dark Matter Halo Structure, *Phys. Rev. D* **87**, 115007 (2013), arXiv:1302.3898 [hep-ph].

[74] B. Colquhoun, S. Heeba, F. Kahlhoefer, L. Sagunski, and S. Tulin, Semiclassical regime for dark matter self-interactions, *Phys. Rev. D* **103**, 035006 (2021), arXiv:2011.04679 [hep-ph].

[75] J. L. Feng, M. Kaplinghat, H. Tu, and H.-B. Yu, Hidden Charged Dark Matter, *JCAP* **07**, 004, arXiv:0905.3039 [hep-ph].

[76] J. L. Feng, M. Kaplinghat, and H.-B. Yu, Halo Shape and Relic Density Exclusions of Sommerfeld-Enhanced Dark

Matter Explanations of Cosmic Ray Excesses, *Phys. Rev. Lett.* **104**, 151301 (2010), arXiv:0911.0422 [hep-ph].

[77] S. Khrapak, Classical scattering in strongly attractive potentials, *Phys. Rev. E* **89**, 032145 (2014), arXiv:1403.6000 [physics.chem-ph].

[78] L. Sagunski, S. Gad-Nasr, B. Colquhoun, A. Robertson, and S. Tulin, Velocity-dependent Self-interacting Dark Matter from Groups and Clusters of Galaxies, *JCAP* **01**, 024, arXiv:2006.12515 [astro-ph.CO].

[79] M. S. Fischer, L. Kasselmann, M. Brüggen, K. Dolag, F. Kahlhoefer, A. Ragagnin, A. Robertson, and K. Schmidt-Hoberg, Cosmological and idealized simulations of dark matter haloes with velocity-dependent, rare and frequent self-interactions, *Mon. Not. Roy. Astron. Soc.* **529**, 2327 (2024), arXiv:2310.07750 [astro-ph.CO].

[80] P. Gondolo and G. Gelmini, Cosmic abundances of stable particles: Improved analysis, *Nucl. Phys. B* **360**, 145 (1991).

[81] A. L. Foguel, P. Reimitz, and R. Z. Funchal, Unlocking the inelastic Dark Matter window with vector mediators, *JHEP* **05**, 001, arXiv:2410.00881 [hep-ph].

[82] L. Lopez-Honorez, O. Mena, S. Palomares-Ruiz, and A. C. Vincent, Constraints on dark matter annihilation from CMB observations before Planck, *JCAP* **07**, 046, arXiv:1303.5094 [astro-ph.CO].

[83] S. D. McDermott, H. H. Patel, and H. Ramani, Dark Photon Decay Beyond The Euler-Heisenberg Limit, *Phys. Rev. D* **97**, 073005 (2018), arXiv:1705.00619 [hep-ph].